Transverse Spin Dynamics in the Anisotropic Heisenberg Model Realized with Ultracold Atoms

Paul Niklas Jepsen,[1,2,3,*] Wen Wei Ho,[3,4,5] Jesse Amato-Grill,[1,2,3,6] Ivana Dimitrova,[1,2,3,4] Eugene Demler,[3,4,7] and Wolfgang Ketterle[1,2,3]

[1]*Department of Physics, Massachusetts Institute of Technology, Cambridge, Massachusetts 02139, USA*
[2]*Research Laboratory of Electronics, Massachusetts Institute of Technology, Cambridge, Massachusetts 02139, USA*
[3]*MIT-Harvard Center for Ultracold Atoms, Cambridge, Massachusetts 02139, USA*
[4]*Department of Physics, Harvard University, Cambridge, Massachusetts 02138, USA*
[5]*Department of Physics, Stanford University, Stanford, California 94305, USA*
[6]*QuEra Computing Inc., Boston, Massachusetts 02135, USA*
[7]*Institute for Theoretical Physics, Wolfgang-Pauli-Strasse 27, ETH Zurich, 8093 Zurich, Switzerland*

(Received 14 March 2021; accepted 23 August 2021; published 17 December 2021)

In Heisenberg models with exchange anisotropy, transverse spin components are not conserved and can decay not only by transport, but also by dephasing. Here, we utilize ultracold atoms to simulate the dynamics of 1D Heisenberg spin chains and observe fast, local spin decay controlled by the anisotropy. However, even for isotropic interactions, we observe dephasing due to a new effect: an effective magnetic field created by superexchange. If spatially uniform, it leads only to uniform spin precession and is, therefore, typically ignored. However, we show through experimental studies and extensive numerical simulations how this superexchange-generated field is relevant and leads to additional dephasing mechanisms over the exchange anisotropy: There is dephasing due to (i) inhomogeneity of the effective field from variations of lattice depth between chains; (ii) a twofold reduction of the field at the edges of finite chains; and (iii) fluctuations of the effective field due to the presence of mobile holes in the system. The latter is a new coupling mechanism between holes and magnons. All these dephasing mechanisms have not been observed before with ultracold atoms and illustrate basic properties of the underlying Hubbard model.

DOI: 10.1103/PhysRevX.11.041054

Subject Areas: Atomic and Molecular Physics
Condensed Matter Physics, Magnetism

I. INTRODUCTION

The famous Heisenberg Hamiltonian, also called the Heisenberg–Dirac–van Vleck Hamiltonian [1–3], describes localized particles on a lattice interacting via spin-exchange couplings. Despite its apparent simplicity, it serves as a paradigmatic model for a host of emergent phenomena, such as ferromagnetism (due to Coulomb exchange, also called potential or direct exchange), antiferromagnetism (due to kinetic exchange from tunneling, also called superexchange) [4], and spin-glass physics [5], as well as exotic states of matter like topologically ordered quantum spin liquids [6]. The dynamics of such models is also very rich and multifaceted and is under active, intense investigation. For example, in one dimension, Heisenberg spin models (with spin quantum number $S = 1/2$) have the special property of being integrable, whereby stable quasiparticles exist at all temperatures. This gives rise to a breakdown of simple hydrodynamics with accompanying varied spin transport behaviors [7–11]. Understanding this has led to the recent development of a theory of generalized hydrodynamics [12,13]. In higher dimensions, the interplay of spontaneous symmetry breaking can lead to long-lived, metastable, prethermal states in addition to the onset of regular spin diffusion [14–16] or even turbulent relaxation with universal scaling of spin-spin correlations [17].

Ultracold atoms in optical lattices form an ideal platform to realize Heisenberg spin models and probe their dynamics in a controlled fashion [18]. In deep lattices where atoms are localized and Mott insulators form [19], superexchange processes via second-order tunneling yield effective Heisenberg spin models, with potential tunability of the strength, sign, and anisotropy of the spin-exchange interactions [20–23]. Until very recently, all experimental studies addressed the special case of an isotropic Heisenberg model [24–31]. However, in Ref. [32], we show how to overcome this limitation and implement Heisenberg models with *tunable* anisotropy of the nearest-neighbor spin-spin couplings, by using ^{7}Li and varying the interactions through Feshbach resonances. We are able to show that the anisotropy profoundly changes the nature of transport of longitudinal

*jepsen@mit.edu

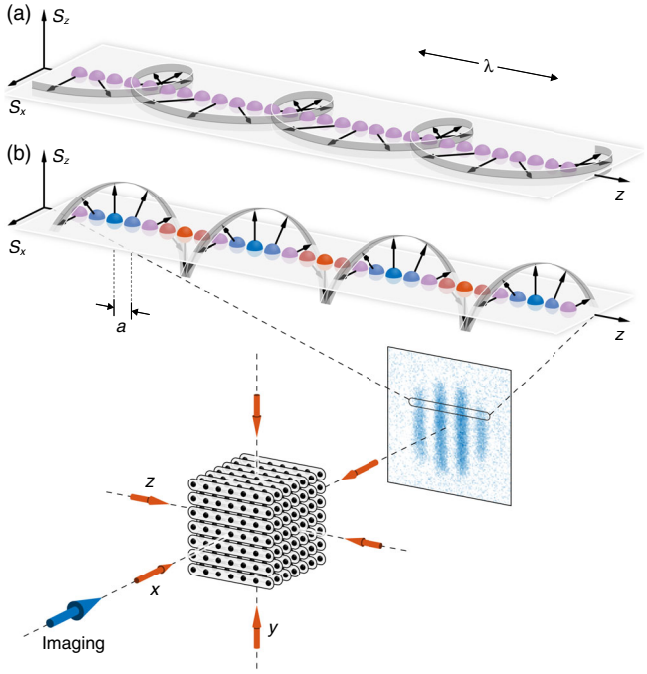

FIG. 1. Geometry of the experiment. The initial state is a transverse (a) or longitudinal (b) spin helix where the spin vector winds within the S_x-S_y plane (a) or S_z-S_x plane (b). The transverse helix (a) is a pure phase modulation of spin $|\uparrow\rangle$ and $|\downarrow\rangle$ states, whereas the longitudinal helix (b) also involves population modulation. Deep optical lattices along the x and y directions create an array of independent spin chains. The z lattice is shallower and controls spin dynamics along each chain.

spin components after a quantum quench from a so-called longitudinal spin helix [Fig. 1(b)] and observe ballistic, subdiffusive, diffusive, and superdiffusive behavior in different parameter regimes. These results bear some similarities with those of spin transport close to equilibrium but strikingly differ in other aspects, prompting the need for further theoretical investigation.

In this paper, we study the relaxation of transverse spin components after quantum quenches from a transverse spin helix [Fig. 1(a)] and observe even more dramatic effects of the anisotropy. In the classical limit, *any* transverse spin helix for *any* anisotropy is stationary, since the torques exerted on a given spin by its neighboring spins cancel exactly (see the Appendix C 1). Therefore, what we study here are the effects of quantum fluctuations on their stability. In contrast to longitudinal spin patterns, which can decay only by transport, transverse spin components can decay also by dephasing. We focus here on two paradigmatic models, which represent complementary spin physics: the XX model, which has only transverse spin-spin couplings and can be mapped to a noninteracting system of fermions, and the XXX model, which has isotropic spin couplings. For the XX model, we observe and explain that the decay is faster for spin-helix patterns with longer wavelengths, in strong contrast to spin transport, where slower dynamics occurs for longer modulations. We also identify several dephasing mechanisms not discussed before. For the XXX model, we identify a symmetry-breaking term in the Bose-Hubbard model: an effective magnetic field caused by different scattering lengths for the spin $|\uparrow\rangle$ and spin $|\downarrow\rangle$ states. This superexchange-induced effective magnetic field is often ignored, since a spatially uniform field can be eliminated in the bulk by going into an appropriate corotating frame. Here, we show that the presence of the effective field is actually significant and gives rise to three additional dephasing mechanisms, all of which more or less contribute equally, resulting in drastically different decay behavior of spin-helix patterns with different orientations, i.e., transverse or longitudinal. (Both would have naïvely been expected to decay with identical timescales for isotropic spin interactions.) One is an inhomogeneous effect where the effective magnetic field is nonuniform between different chains in our sample. This can be eliminated with a spin-echo technique. The second is due to dephasing occurring at the ends of finite chains. The third is due to the presence of mobile holes resulting in a fluctuating effective magnetic field in the bulk, i.e., a hole-magnon coupling.

Our work shows the limitations of a pure spin model in capturing spin dynamics realized with ultracold atoms and demonstrates the need for a theoretical model explicitly featuring hole-magnon couplings (the so-called bosonic $\tilde{t}$-J model) in order to reach a more complete description of experiments. The new insight into hole-magnon coupling should be important for other systems and materials where such couplings are present, such as high-temperature superconductors [33–35].

II. EXPERIMENTAL METHODS

The spin models are implemented with a system of two-component bosons in an optical lattice, which is well described by the Bose-Hubbard model. These two states (lowest and second-lowest hyperfine states of ^{7}Li), labeled $|\downarrow\rangle$ and $|\uparrow\rangle$, form a spin-1/2 system. In the idealized scenario of a Mott insulating regime at unity filling, bosons cannot tunnel, and the effective Hamiltonian for the remaining spin degree of freedom is given by the spin-1/2 Heisenberg XXZ model [20–23]:

$$H = \sum_{\langle ij \rangle} \left[J_{xy}(S_i^x S_j^x + S_i^y S_j^y) + J_z S_i^z S_j^z - \frac{h_z}{2}(S_i^z + S_j^z) \right], \quad (1)$$

where S^x, S^y, and S^z are the spin-1/2 Pauli operators and the sum is over nearest-neighbor pairs of sites $\langle ij \rangle$. In leading order, one obtains for the transverse coupling $J_{xy} = -4\tilde{t}^2/U_{\uparrow\downarrow}$ and for the longitudinal coupling $J_z = 4\tilde{t}^2/U_{\uparrow\downarrow} - (4\tilde{t}^2/U_{\uparrow\uparrow} + 4\tilde{t}^2/U_{\downarrow\downarrow})$, both mediated by superexchange. Here, $\tilde{t}$ is the tunneling matrix element between neighboring sites, while $U_{\uparrow\uparrow}$, $U_{\uparrow\downarrow}$, and $U_{\downarrow\downarrow}$ are

the on-site interaction energies. The effective magnetic field strength is $h_z = 4\tilde{t}^2/U_{\uparrow\uparrow} - 4\tilde{t}^2/U_{\downarrow\downarrow}$. Note that the total magnetization $\sum_i S_i^z$ in the S_z direction is conserved by the Hamiltonian.

The magnitude of superexchange can be varied over 2 orders of magnitude by changing the lattice depth, which scales the entire Hamiltonian. The anisotropy $\Delta \coloneqq J_z/J_{xy}$ is controlled via an applied magnetic field which tunes the interactions through Feshbach resonances in the lowest two hyperfine states. In the regime studied here, the transverse coupling is positive ($J_{xy} > 0$). The ability to tune the anisotropy over a wide range of values, both positive and negative, allows us to explore dynamics beyond previous experiments [24–28] in which $\Delta \approx 1$.

One-dimensional (1D) chains are created by two perpendicular optical lattices whose depths $V_x, V_y = 35E_R$ are sufficient to prevent superexchange coupling on experimental timescales. A third orthogonal lattice along the z direction with adjustable depth V_z controls the superexchange rate in the chains (Fig. 1). Here, $E_R = h^2/(8ma^2)$ denotes the recoil energy, where $a = 0.532$ μm is the lattice spacing, m the atomic mass, and h Planck's constant. After preparing a transverse spin helix [Fig. 1(a); this work] or a longitudinal spin helix [Fig. 1(b); as in our previous work [32]] with wavelength λ (and wave vector $Q = 2\pi/\lambda$) in each chain [27,36,37], time evolution is initiated by rapidly lowering V_z. The dynamics following this quench is then (approximately) governed by the 1D XXZ model Eq. (1). After an evolution time t, the dynamics is frozen by rapidly increasing V_z, and the atoms are imaged in the $|\uparrow\rangle$ state via state-selective polarization-rotation imaging with an optical resolution of about six lattice sites. For imaging the transverse spin, we apply a $\pi/2$ pulse first, so that we observe the magnetization in the S_x direction. To distinguish homogeneous from inhomogeneous dephasing, we can use a spin echo by applying a π pulse (with a typical duration of $t_\pi = 150$ μs $\ll \hbar/J_{xy}$) after half of the evolution time t.

Integrating the images along the direction perpendicular to the chains yields a 1D spatial profile of the population in the $|\uparrow\rangle$ state, averaged over all spin chains. As in Fig. 1, the spin helix exhibits a sinusoidal spatial modulation of the density of $|\uparrow\rangle$ atoms, observed as a characteristic stripe pattern with a normalized contrast $c(t)$. During the evolution time t, the 100% contrast of the initial spin helix decays, and we determine the dependence of $c(t)$ on lattice depth V_z, wave vector Q, and anisotropy Δ. Analyzing each decay curve $c(t)$ yields a decay rate γ, among other fit parameters (see Fig. 6 in Appendix A for data fitting methods).

In general, we measure the spin dynamics at two or more different lattice depths V_z and verify that the decay curves $c(t)$ collapse when time is rescaled by the corresponding spin-exchange time $\hbar/J_{xy}$, confirming that the dynamics is driven by superexchange. These time units are obtained from the experimentally determined lattice depth using an extended Hubbard model (detailed in Ref. [32]).

III. RESULTS

A. XX model

We first consider a very anisotropic system by realizing the Heisenberg model tuned to the noninteracting point ($\Delta = 0$) and study the decay of the transverse spin helix for different wave vectors Q [Figs. 2(a) and 2(b)]. We find the decays are quick, all having timescales on the order of a few spin-exchange times $\hbar/J_{xy}$, much faster than the decay of the longitudinal spin helix which is driven by ballistic transport. Importantly, the transverse decay rate even *increases for longer wavelengths* of the helix, showing that the decay is not caused by transport where magnetization redistributes in space and equilibrates, for which we would expect slower rates for longer modulations, but by dephasing where magnetization is locally created or removed.

Some insight into the fast timescales of transverse decay is obtained by taking the $Q \to 0$ limit, where the initial state becomes a uniformly polarized state. This state is obviously not an eigenstate of the quantum XX model and is, therefore, unstable. Further simplification to a two-site (double-well) system allows us to analytically diagonalize the Heisenberg Hamiltonian, which gives a level structure as shown in Fig. 2(c) (for $h_z = 0$). When $\Delta = 1$, the transverse spin state $|\rightarrow\rightarrow\rangle \coloneqq (|\uparrow\rangle + |\downarrow\rangle)(|\uparrow\rangle + |\downarrow\rangle)/2$ is an eigenstate of the Hamiltonian as all triplet states are degenerate and, hence, does not evolve. However, for $\Delta \neq 1$, the degeneracy is lifted, and the state $|\rightarrow\rightarrow\rangle$ shows a beat note at the frequency of the energy splitting $J_{xy}(1-\Delta)/2$. For $\Delta = 0$, this indicates a dephasing time for transverse spins on the order of a few spin-exchange times $\hbar/J_{xy}$, in qualitative agreement with our observations. For many sites, there will be a spectrum of beat frequencies leading to irreversible dephasing locally.

We can explain the unusual Q dependence of the experimentally observed transverse decay with a semiclassical analysis of spin dynamics (see Appendices C 1 and C 2). In the classical limit, spin-helix states satisfy the Landau-Lifshitz equations of motion $\partial_t \vec{S}_i(t) = (\partial H/\partial \vec{S}_i) \times \vec{S}_i(t) = 0$ for any wave vector Q and, therefore, do not decay (this is, in fact, true for any anisotropy Δ), because the torques exerted on $\vec{S}_i$ by its neighbors cancel exactly. Here, $\vec{S}_i$ is a classical spin vector, which corresponds to the $S \to \infty$ limit of a quantum mechanical spin. For finite S, we can study the effects of quantum fluctuations with a large spin $(1/S)$ expansion. We find that the Fourier modes of the fluctuations carrying momentum k have a dispersion relation $\omega_k \propto J_{xy}|\cos(Qa)\sin(ka/2)|$. As the characteristic energy scales of all modes are proportional to $|\cos(Qa)|$, this indicates, in a somewhat surprising fashion, that the dynamics of the spin helix is faster for longer wavelengths than for smaller wavelengths. The slowest dynamics occurs at $Qa = \pi/2$ (or $\lambda = 4a$), where neighboring spins are at an angle of 90°. This state is robust (at least to leading order)

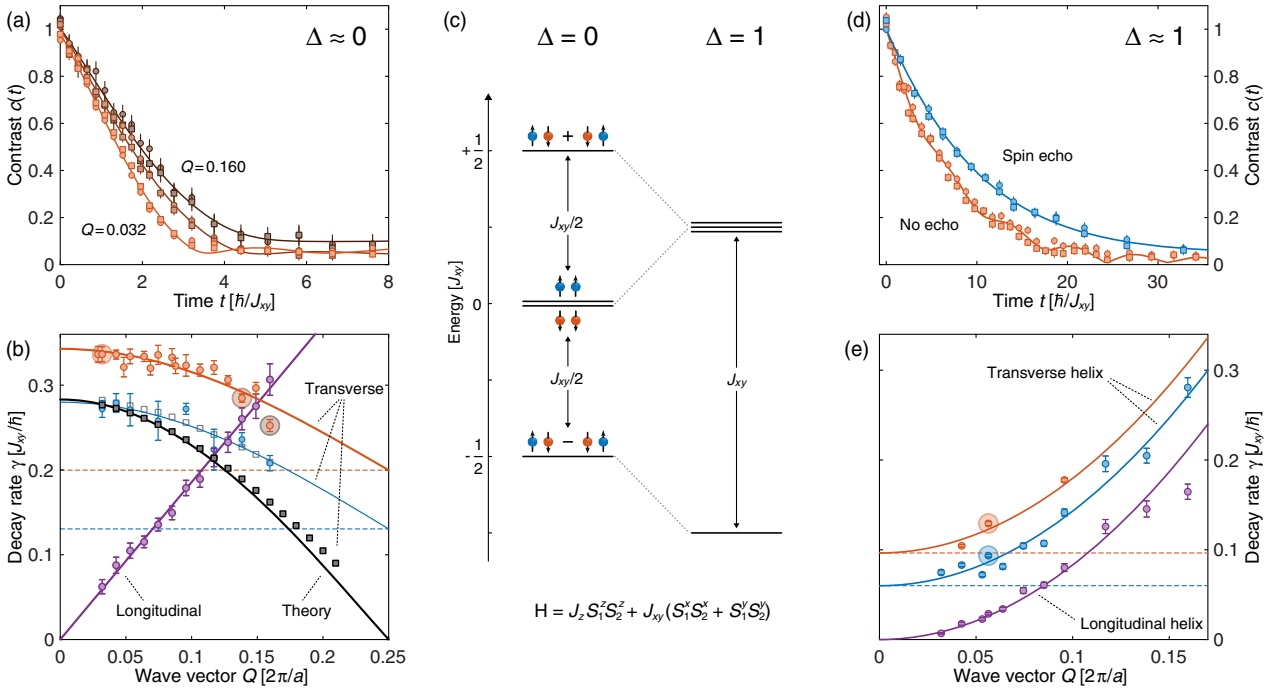

FIG. 2. Spin dephasing and spin transport for the XX model [$\Delta \approx 0$, (a),(b)] and the isotropic XXX model [$\Delta \approx 1$, (d),(e)]. (a) Spin relaxation at $\Delta \approx 0$. Transverse spin-helix contrast $c(t)$ for $Qa = 2\pi \times 0.032$, 0.138, and 0.160 (bright to dark orange). The curves for different lattice depths $11E_R$ (○) and $13E_R$ (□) collapse when times are rescaled in units of the corresponding spin-exchange times $\hbar/J_{xy} = 1.71$ (○) and 4.30 ms (□). The transverse spin decays on a timescale of a few spin-exchange times which increases for smaller wavelengths $\lambda = 2\pi/Q$. (b) Wave-vector dependence. The initial decay rates [orange points; with values from (a) highlighted] follow a cosine dependence $\gamma(Q) = \gamma_1 \cos(Qa) + \gamma_0$ (solid orange line) with a constant background rate $\gamma_0 = 0.20(2)J_{xy}/\hbar$ (dashed orange line). This is in strong contrast to the longitudinal spin helix (purple) which shows linear scaling with Q (indicating ballistic transport). A spin echo (π pulse at time $t/2$) reduces the background rate to $\gamma_0 = 0.13(3)J_{xy}/\hbar$ (dashed blue line). The black solid squares are numerical results for a single chain and the defect-free XX model (with $h_z = 0$) with a fit $\gamma(Q) = \gamma_1 \cos(Qa)$ (solid line) to the points with $Qa \leq 2\pi \times 0.075$. The gray open squares are numerical results for the $\tilde{t}$-J model with 5% hole fraction (see Appendix E 1). (c) Energy levels of the Heisenberg Hamiltonian for two spins in a double-well potential. For $\Delta \neq 1$, the triplet states are split. (d) Spin relaxation at $\Delta \approx 1$. Transverse spin-helix contrast $c(t)$ for $Qa = 2\pi \times 0.056$ without spin echo (orange) and with spin echo (blue). The difference shows the presence of inhomogeneous dephasing. The curves taken for different lattice depths $11E_R$ (○) and $13E_R$ (□) collapse when times are rescaled in units of the corresponding spin-exchange times $\hbar/J_{xy} = 2.55$ (○) and 6.42 ms (□). (e) Wave-vector dependence. Decay rates for the transverse helix [orange and blue points; with values from (d) highlighted] and longitudinal helix (purple points), for $\Delta \approx 1$. The orange (no echo) and blue (with echo) solid lines are fits $\gamma(Q) = DQ^2 + \gamma_0$ assuming two contributions to the decay rate: one quadratic term (indicating diffusive transport) with diffusion constant D (taken from the longitudinal spin dynamics shown in purple), the other Q-independent γ_0 (shown by the dashed lines). The spin echo reduces the background decay rate γ_0 by an amount of $0.036J_{xy}/\hbar$ (e) and $0.069J_{xy}/\hbar$ (b). These values are consistent with an inhomogeneous dephasing rate proportional to the effective magnetic field h_z, with (predicted) values $h_z = 0.89J_{xy}$ (e) and $1.43J_{xy}$ (b).

against decay induced by quantum fluctuations, because the fluctuations of a spin which points, e.g., in the S_x direction are in the S_y-S_z plane and, for $\Delta = 0$, do not cause any precession of their immediate neighboring spins (which point along the $\pm S_y$ direction).

This prediction is furthermore corroborated by a fully quantum ($S = 1/2$) but short-time expansion of the order parameter of the spin helix (see Appendix C 3). Numerical simulations, as seen in Figs. 2(b) and 8(a), also verify this by showing a very good collapse of the decay curves of all experimentally considered wave vectors Q upon rescaling time by a factor of $\cos(Qa)$. This holds even up to evolution times t longer than would be expected to be valid for the semiclassical analysis or short-time expansion. Unsurprisingly, deviations from this relation are seen as the wave vector approaches $Q = \pi/(2a)$, for which the simple approaches would predict a vanishing decay rate. However, note that the transverse spin helix with $Q = \pi/(2a)$ can be shown to be an exact eigenstate of the XX model with appropriate boundary conditions [38,39].

Experimentally, we find that the decay rate of the transverse helix as a function of wave vector Q can be fitted very well as the sum of the predicted $\cos(Qa)$ dependence together with a constant term, as shown in

Fig. 2(b). The constant term represents additional dephasing mechanisms that go beyond the idealizations of the spin model (1), which we discuss below.

B. *XXX* model

When $\Delta = 1$, we realize the isotropic Heisenberg spin model which, aside from the effective magnetic field h_z, satisfies $[H, \sum_i S_i^\alpha] = 0$ ($\alpha = x, y, z$). The presence of the effective magnetic field term $\sum_{\langle ij \rangle}(h_z/2)(S_i^z + S_j^z)$ in Eq. (1), which we can rewrite as $\sum_i h_{z,i} S_i^z$, explicitly breaks this spin-rotational symmetry. Now, a uniform (i.e., site-i-independent) field $h_{z,i}$ can be transformed away by going into an appropriate rotating frame. In such a case, the transverse and the longitudinal spin helix should show exactly the same dynamical behavior.

However, as the results in Figs. 2(d) and 2(e) show, there is a dramatic difference: The transverse helix decays much faster than the longitudinal helix with the same wave vector Q. In particular, the longitudinal helix exhibits a purely diffusive scaling with wave vector Q; i.e., its decay rate obeys $\gamma(Q) = DQ^2$, where D is a diffusion constant (as shown in Ref. [32]), whereas the transverse helix has an additional Q-independent decay rate of $\gamma_0 = 0.096(10) J_{xy}/\hbar$, with the net decay rate fitted well by $\gamma(Q) = DQ^2 + \gamma_0$. This lends naturally to the interpretation that the system at this point realizes dynamics close, but not equal, to a model where global transverse magnetization is exactly conserved. In other words, there is not only a transport channel under which the transverse helix decays by, such that local magnetization profiles redistribute in space and eventually equilibrate, but also a nontransport (dephasing) channel, whereby transverse magnetization can be created or removed locally, arising from explicit symmetry-breaking terms. (Note that for the highly anisotropic case $\Delta = 0$ we cannot separate out such a transport part.)

In the following, we discuss and quantify three plausible mechanisms leading to such dephasing. First, a careful read of the Hamiltonian Eq. (1) indicates that the effective magnetic field $h_{z,i}$ is *explicitly* nonuniform for systems of finite sizes, as encountered in experiments. This stems from the fact that all terms in the Hamiltonian arise from superexchange, which requires *pairs* of sites, and that sites at the edges of the system have fewer neighbors than sites in the bulk (discussed further below). Hence, relevant symmetry-breaking terms (i.e., which cannot be transformed away) are already present in the idealized spin model. Second, our experiment consists of an *ensemble* of 1D systems, and there is a small inhomogeneity in the effective magnetic field strengths between chains due to slight variations in the lattice depth caused by the Gaussian shape of the laser beam. This can lead to a loss of measured (ensemble-averaged) contrast due to destructive interference from spins precessing at different rates, leading to a Q-independent decay rate. Third, a natural deviation of our experiment from the idealized spin physics governed by the pure Heisenberg Hamiltonian Eq. (1) is the presence of a small fraction of mobile holes in the spin chains caused by nonadiabatic preparation of the Mott insulator and nonzero temperature. Typical hole fractions lie between 5% and 10% in the central part of the Mott insulator [27,32]. In a simplified picture, holes cause dephasing, because spins next to holes experience only half the effective magnetic field. A mobile hole, therefore, creates a fluctuating effective magnetic field, causing dephasing of the transverse spin component. Below, we present experimental studies and extensive numerical simulations which find that all of these effects contribute roughly equally a Q-independent decay rate.

We note also that, in the final data analysis, a reevaluation of the scattering lengths shows that our data is actually not taken exactly at the isotropic point but at $\Delta = 0.93 \pm 0.05$. This deviation from isotropy is responsible for a Q-independent decay rate of $0.015 J_{xy}/\hbar$, or 15% of the observed difference between longitudinal and transverse spin decay (Appendix E 3). When all these effects are taken together, this accounts approximately for the experimentally measured Q-independent decay rate γ_0 for the transverse helix.

C. Imaging the effective magnetic field

All the symmetry-breaking mechanisms we discuss above involve the effective magnetic field. Therefore, we first present how this field can be directly observed and quantified.

If we assume that the ensemble experiences two pronounced values of the effective magnetic field, then the time evolution of the cloud-averaged contrast $c(t)$ will show a beat note at a frequency which corresponds to the difference of the two values of the effective magnetic field. This is the case for our atom clouds, which feature a Mott insulator plateau surrounded by a dilute shell of individual atoms [32] which are pinned to their lattice sites by the gradient of the harmonic trapping potential [40]. Many of these individual atoms do not have neighbors for spin exchange and, therefore, do not feel an effective magnetic field, while those in the Mott insulator plateau do. The observed beat frequencies $\Omega = 0.90(1) J_{xy}/\hbar$ (Fig. 3) agree well with the predicted value of the superexchange-generated effective magnetic field $h_z = 0.89 J_{xy}$. As expected, the beat note is more pronounced by spatially selecting the outer parts of the cloud [Fig. 3(a)] and disappears with a spin echo [Fig. 2(d)]. In Appendix B, we describe an alternate spectroscopic method to observe the effective magnetic field as a shift in the spin-flip frequency.

The presence of the effective magnetic field can also be directly imaged by introducing a sufficiently large gradient in the lattice depth between the chains. This can be achieved by vertically displacing the z lattice relative to the atom cloud (see Fig. 1), causing a gradient of the effective magnetic field. As this field sets the "spiraling" frequencies of the individual spin helices across the cloud (simply arising from the on-site precession of the spins

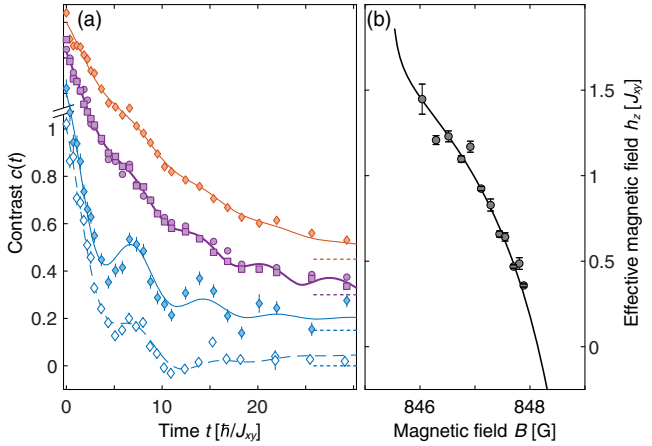

FIG. 3. Absolute measurement of the effective magnetic field value h_z as a beat note between the spin precession frequencies in the inner and outer parts of the cloud. (a) Transverse spin-helix contrast $c(t)$ for $\lambda = 23.5a$ (all filled symbols) and $\Delta \approx 1$. For measurements averaged over the whole atom cloud (purple), they are performed at $11E_R$ (○) and $13E_R$ (□). The contrast at the center of the atom cloud for radii $r \leq 8.5a$ (orange filled symbols) decays slower with less pronounced oscillations, whereas the contrast in the spatial wings for radii $r \geq 20a$ (blue filled symbols, including approximately 7% of the atoms in the cloud) decays faster with more pronounced oscillations. Data points for diamonds are an average of measurements at $11E_R$ and $13E_R$. Open diamond symbols represent data for $\lambda = 10.4a$ and show the same oscillation frequency but decay faster due to spin transport. Lines are fits described in Appendix A. Curves are offset from each other for clarity. The dotted lines indicate their respective zeros. (b) The beat frequency Ω varies as a function of the externally applied magnetic field B. The measured values for $\hbar\Omega$ (points) follow the theoretical prediction (without any adjustable parameter) for the effective magnetic field h_z (solid line) which is tuned by varying the scattering lengths via Feshbach resonances.

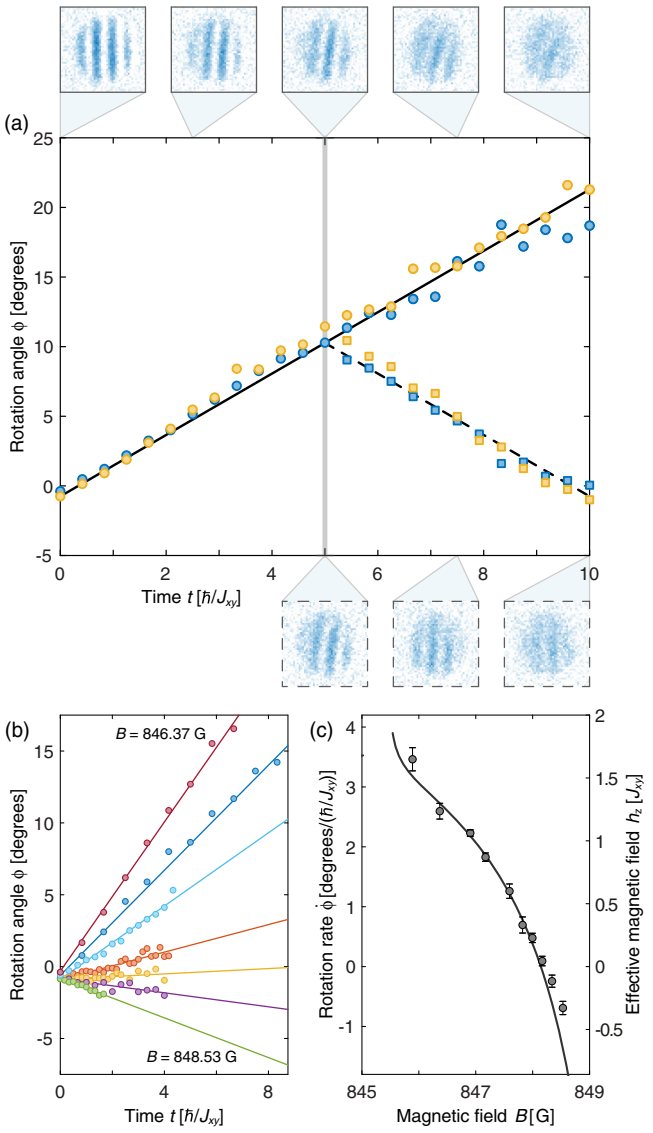

FIG. 4. Direct observation of the effective magnetic field through spin precession. (a) Rotation angle of the stripe pattern as a function of evolution time t (filled symbols) for two lattice depths $11E_R$ (blue) and $13E_R$ (yellow) without (solid line) and with (dashed line) spin-echo pulse at $t = 5\hbar/J_{xy}$. (b),(c) Tunability of the effective magnetic field h_z. (b) Rotation angle as a function of evolution time t for different magnetic fields $B =$ 846.37 (red), 847.17 (blue), 847.59 (light blue), 848.00 (orange), 848.17 (yellow), 848.34 (purple), and 848.53 G (green). (c) Angular velocities obtained from linear fits in (b) compared to predicted effective magnetic fields h_z (solid line) with the scale factor between the two y axes as a fitting parameter yielding $\dot{\phi}\hbar/J_{xy} = 0.037h_z/J_{xy} = 2.1°h_z/J_{xy}$, representing the (uncalibrated) gradient of the lattice depth. Times are normalized by the spin-exchange time $\hbar/J_{xy}$ for the central part of the atom cloud. The scaling factor is consistent with a displacement of the z-lattice beam ($1/e^2$ radius of 125 μm) by an amount of 29 μm $= 55a$.

about the S_z axis), this translates to an observable tilt of the whole stripe pattern [Fig. 4(a)].

The tilt angle grows linearly in time, with a rate proportional to the effective magnetic field and the gradient of the lattice depth (which we keep fixed). Externally applied magnetic fields change the scattering lengths via broad Feshbach resonances, and so we can tune the effective magnetic field. The observed rates for the tilt rotation versus applied magnetic field B are shown in Figs. 4(b) and 4(c) and agree well with our theoretical prediction. In particular, near $B = 848.1$ G, the spin $|\uparrow\rangle$ and $|\downarrow\rangle$ scattering lengths are identical $a_{\uparrow\uparrow} = a_{\downarrow\downarrow}$ and the effective magnetic field is zero, evinced by the absence of any tilt in time [Fig. 4(b); yellow data points].

We note that, in principle, such a rotation could also be caused by an external magnetic field gradient. However, the tilt angle would then not depend on the lattice depth V_z and

the external magnetic field B. In a sufficiently deep lattice ($V_z = 35E_R$), for up to at least 40 ms, we do not observe any discernible rotation, hence ruling out an external field gradient.

When an echo pulse is added, the direction of the stripe rotation is reversed, and, at twice the echo time, the stripe pattern is vertical again, resulting in high contrast for vertically integrated images [Fig. 4(a); bottom]. This shows how the spin echo eliminates the effect of inhomogeneous effective fields across the cloud, a technique we use below to quantify their contribution to the dephasing of transverse spin patterns.

D. Dephasing mechanisms for the transverse spin helix

We now elaborate on and quantify the effects of three possible dephasing mechanisms we identify, induced by the effective magnetic field.

1. Effect of inhomogeneity in the effective magnetic field between chains

The effect of inhomogeneity in the effective magnetic field strengths between chains in the ensemble, arising from slight variations in the lattice depth from the Gaussian nature of the laser beams, can be eliminated by applying a spin-echo pulse at half of the evolution time t.

Indeed, when adding spin-echo pulses to the experimental sequence, we find the Q-independent background decay rate γ_0 is reduced from 0.096(10) to $0.060(3)J_{xy}/\hbar$ [dashed lines in Fig. 2(e)]. This is compatible with an effective magnetic field distribution over different chains with a full width at half maximum (FWHM) of 8.2%, corresponding to variations in the lattice depth V_z of 1.6%, compatible with experimental parameters.

2. Effect of finite chain lengths

As noted before, the effective magnetic field of the ideal Heisenberg Hamiltonian Eq. (1) is necessarily nonuniform for systems of finite sizes. To elaborate, the effective magnetic field arises from superexchange involving nearest-neighbor pairs of atoms, indicated already in the Hamiltonian Eq. (1), where we deliberately write the magnetic field $\sum_{\langle ij\rangle}(S_i^z + S_j^z)$ as a sum over pairs $\langle ij\rangle$ of sites to emphasize this fact. This means, in particular, that, for a 1D chain, the effective magnetic field is reduced to $h_z/2$ at the ends, half the value in the bulk. For $h_z \neq 0$, this nonuniformity hence cannot simply be transformed away by going into an appropriate corotating frame. Although this reduced field is localized at the ends of the chain, it cannot be eliminated with an echo protocol, since its effect propagates along the chain via spin dynamics as illustrated in Fig. 10 (note the echo pulse removes inhomogeneous dephasing only for subsystems, which do not interact with each other, such as separate chains in the ensemble).

This edge effect results in differences in the relaxation between the transverse and the longitudinal spin helix: The spins at the edges dephase rapidly, and this perturbation then propagates through the entire chain. We perform numerical simulations which show that, for chain lengths of 10–20 spins, the edge effect causes a dephasing rate of approximately $0.02J_{xy}/\hbar$ (Appendix E 4). Although the diameter of the Mott insulator plateau we experimentally realize is measured to be around 40 sites, we expect that holes (with an estimated concentration of 5%–10%) [27,32] in the outer region of the Mott plateau are localized by the gradient of the trapping potential and create effectively shorter chains in our sample. In contrast to that, in the central region of the Mott plateau, where the trapping potential is flat, holes are mobile, and their effect is discussed below.

The edge effect can be viewed as an inhomogeneity of the effective magnetic field realized within a single chain. In addition to this effect, we have a harmonic trapping potential in the experimental system, which along a given chain creates an additional inhomogeneity, since it creates an energy offset between neighboring sites and modifies the superexchange rate by up to approximately 10% (see the methods section in Ref. [32] for details). We estimate that this is somewhat less important than the effect of the 50% reduced effective field at the ends of the chain.

3. Effect of mobile holes

We now explore a dephasing mechanism beyond the pure spin model, namely, the presence of mobile holes in the system. For negligible interactions, the dynamics of holes can be described by a quantum random walk where the time-dependent wave function at site i for a hole initially localized at $i = 0$ is the Bessel function $J_i(t/(\hbar/2\tilde{t}))$. The square of the Bessel function shows oscillations at frequencies $\omega = 4\tilde{t}/\hbar$ or periods of $T = (\pi/2)\hbar/\tilde{t}$. Now, for a hold time T and with an echo pulse at $T/2$ (described in the previous subsection), those fluctuations are "rectified" and lead to enhanced dephasing (note that the spin echo removes stationary inhomogeneous magnetic fields but can enhance the effect of time-dependent fluctuations [41]). This is evidence for hole-magnon coupling: Holes carry a localized magnetic field which couples to spin dynamics. Indeed, Fig. 5 shows a feature in the spin-echoed contrast at early times on the order of the tunneling time $\hbar/\tilde{t}$ in accordance with these predictions, providing experimental evidence that mobile holes are possibly present. By using a series of echo pulses at frequency ω, one could map out the frequency spectrum of the effective magnetic field, using concepts from dynamic decoupling [41].

For times on the order of superexchange scales, the effect of the hole-induced fluctuating effective magnetic field can be captured by a simple model. From nuclear magnetic resonance, it is well known that the dephasing time T_2 of a localized spin at $z = 0$ is related to the magnetic field fluctuations h_z (measured in units of energy) and their coherence time τ_c via $1/T_2 = \langle h_z^2\rangle\tau_c/\hbar^2 = G(z=0,\omega=0)/\hbar^2$,

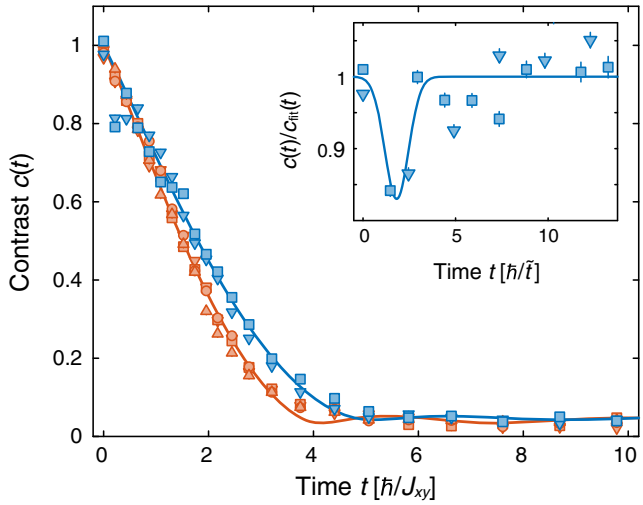

FIG. 5. Tunneling dynamics of mobile holes. Decay curves for the XX model ($\Delta \approx 0$) at $\lambda = 10.4a$ without a spin-echo pulse (orange) and with a spin-echo pulse (blue) after half the evolution time t, measured for different lattice depths $9E_R$ (△), $11E_R$ (○), $13E_R$ (□), and $15E_R$ (▽). The time axis has units of the corresponding spin-exchange times $\hbar/J_{xy} = 0.64$ (△), 1.71 (○), 4.30 (□), and 10.29 ms (▽). Solid lines are fits (see Appendix A). The spin echo generally slows down relaxation slightly by eliminating inhomogeneous dephasing, except at early times where relaxation is actually enhanced and the data points reproducibly deviate from the solid line (data points at $t = 0.22$ and $0.43\hbar/J_{xy}$ have to be excluded from fitting). The inset shows the data points divided by the fit function and plotted with time in units of the tunneling time $\hbar/\tilde{t}$, showing enhanced relaxation around 1–2 tunneling times (the solid line is a guide for the eye). More extensive studies with higher time resolution reproduce similar features at around the tunneling time, but their shape is sensitive to experimental conditions, including the atom number.

where $G(z,t) = \langle h_z(z,t)h_z(0,0)\rangle$ is the autocorrelation of the fluctuating magnetic field along the chain [42]. The dephasing time T_2 is the same for spin patterns with arbitrary wave vector Q.

For a moving hole, the effective magnetic field has a correlation function $G(z,t)$ which is identical to the (normalized) density-density correlation function $J(z,t)$ of the hole, multiplied by h_z^2 [here, we neglect the fact that the effective magnetic field at a given site depends on the holes on the neighboring sites; see Eq. (1)]. For uncorrelated holes with hole probability p, the variance of the local occupation is p with a coherence time $\tau_c = 1.14(\hbar/2\tilde{t})$, where $\tilde{t}$ is the tunneling matrix element [43]. The associated correlations of the fluctuating effective magnetic field determine the T_2 dephasing time for the spin helix $1/T_2 = 0.57h_z^2 p/\tilde{t}\hbar$. Assuming $p = 0.1$ (10% hole fraction) and using $\tilde{t} = 6.15J_{xy}$ (at $V_z = 11E_R$) and $h_z/J_{xy} = 0.89$, this leads to an estimate of $1/T_2 \approx 0.007J_{xy}/\hbar$.

This simple model of magnon-hole dynamics indicates already the non-negligible effect of a small fraction of holes and strongly suggests that a more generalized model beyond the pure spin Heisenberg model Eq. (1) should be considered. To this end and to substantiate the rough estimate of the dephasing rate from the simple model, we perform simulations of the bosonic $\tilde{t}$-J model which explicitly take into account the presence of holes in the Mott insulator near unity filling. This model allows holes to be present but does not include double occupancies of bosons, since they are suppressed by the large on-site repulsion U. See Appendix F for its explicit form and derivation beginning from the Bose-Hubbard model, as well as an interpretation of its constituent terms in terms of magnon-hole couplings. There, we also show that a nonzero field strength h_z is a *necessary* and *sufficient* condition for the $\tilde{t}$-J model to break spin rotational symmetry, justifying our identification of the effective magnetic field as the agent giving rise to differences in dynamics between the transverse and the longitudinal spin helix.

Numerical simulations using the bosonic $\tilde{t}$-J model for a mobile hole fraction of 10%, with experimentally realized parameters that would yield the XXX model ($\Delta = 1$) in the ideal spin limit, show a Q-independent dephasing at a rate around $0.026J_{xy}/\hbar$ for the experimental conditions in Fig. 2(e) (see Appendix E 2), supporting the simplified model of hole-induced dephasing presented above (but providing a rate 3 times higher). Note that we cannot experimentally measure the hole fraction and use here the typical range of values of 5%–10% observed or inferred in other experiments [27,32].

4. Summary of the dephasing mechanisms

At this stage, we account for the isotropy-breaking dephasing rate of 0.096 (in units of $J_{xy}/\hbar$) through more or less equal contributions from the edge effect (0.020), effective magnetic field inhomogeneity between chains which can be eliminated via spin echo (0.036), and mobile holes (0.013–0.026, assuming a hole fraction p between 5% and 10% and linear dependence on p), as well as a small deviation from isotropy (0.015). These numbers are summarized in Table I. We regard some of the numbers as only semiquantitative due to the nonexponential character of the measured and calculated decay curves, but they indicate which phenomena have to be accounted for in quantum simulations of spin dynamics using ultracold atoms in optical lattices.

5. Revisiting the XX model

Our considerations above illustrate the role of edge effects and a small number of holes in the dephasing of transverse spin. This should also contribute to the dephasing in the XX model. Hence, we revisit it via simulations of the bosonic $\tilde{t}$-J model with the appropriate experimental parameters (see Appendix E 1) and can now account for two experimental findings. For the Q-independent decay rate, we note that the $h_z = 1.43J_{xy}$ term is 1.6 times larger

TABLE I. Q-independent decay rates for different dephasing mechanisms at $\Delta \approx 1$, obtained through experimental studies (spin echo for field inhomogeneity) and extensive numerical simulations (edge effect, mobile holes, and experimental deviation from isotropy). Numbers should be regarded as semiquantitative but, taken as a whole (second last row), strongly suggest that they account for the net decay rate experimentally observed (last row).

Dephasing mechanism	Decay rate ($J_{xy}/\hbar$)
Edge effect	0.020
Field inhomogeneity	0.036
Mobile holes	0.013–0.026
Experimental deviation from $\Delta = 1$	0.015
Total	0.084–0.097
Experimentally measured rate	0.096(10)

compared to our experimental realization of the XXX model, which explains the larger observed Q-independent dephasing rate $\gamma_0 = 0.20(2)J_{xy}/\hbar$ [Fig. 2(b)] semiquantitatively. Furthermore, the simulations show that the amplitude γ_1 of the $\cos(Qa)$ dependence is a function of the concentration of holes [see Figs. 2(b) and 8]. We find that the experimental data agree best with numerical simulations for 5% holes.

IV. CONCLUSIONS

We have used ultracold atoms to implement the Heisenberg model with tunable anisotropy. For the relaxation of transverse spin patterns, we have studied for the first time four decay mechanisms: intrinsic dephasing by anisotropic spin-exchange couplings, inhomogeneous dephasing through a static superexchange-induced effective magnetic field, dephasing through the ends of the chain, and dephasing by a fluctuating effective magnetic field due to the presence of mobile holes. One reason why several of these mechanisms have not been observed before is that most previous studies of spin dynamics in optical lattices have used either fermions [24], for which the $\tilde{t}$-J model is always explicitly spin rotationally symmetric and, therefore, $h_z = 0$, or bosons comprised of ^{87}Rb [25–28], for which the spin $|\uparrow\rangle$ and spin $|\downarrow\rangle$ scattering lengths are almost identical ($a_{\uparrow\uparrow} = 99.0a_0$, $a_{\uparrow\downarrow} = 99.0a_0$, and $a_{\downarrow\downarrow} = 100.4a_0$, with the Bohr radius a_0) [44], leading to a value of $h_z \approx 0.014J_{xy}$, approximately 100 times smaller than for ^{7}Li.

The experimental and theoretical results presented in this work go beyond pure spin physics. They illustrate effects caused by a small hole fraction that is generally present in cold atomic quantum simulators. A more complete description of spin dynamics in such systems, therefore, requires using the $\tilde{t}$-J model, which features magnon-hole couplings.

This coupling between density and spin is analogous to the interplay of spin and charge degrees of freedom in strongly correlated electronic systems, which is important, for example, in understanding emergent many-body phenomena like high-temperature superconductivity in cuprates [33–35]. Therefore, our platform presents an elegant new setting where such physics can be emulated. More generally, we regard our work as a starting point for exploring spin dynamics in different dynamical regimes as well as in generalized Heisenberg models. Experimentally, the effect of mobile holes can be studied by varying the lattice depth over a large range, which affects hole dynamics (tunneling) differently than spin dynamics (superexchange). A quantum gas microscope will be able to select chains of a certain length and to measure spin and hole dynamics with single-site resolution. Exciting future directions include the study of spin polaron dynamics [45], realizing long-lived, metastable prethermal states in higher dimensions [14–16], and probing the onset of turbulent spin relaxation utilizing larger spin quantum numbers [17].

ACKNOWLEDGMENTS

We thank Y. K. Lee and H. Lin for experimental assistance, J. Rodriguez-Nieva for discussions, and J. de Hond for comments on the manuscript. We acknowledge support from the NSF through the Center for Ultracold Atoms and Grant No. 1506369, ARO-MURI Non-Equilibrium Many-Body Dynamics (Grant No. W911NF-14-1-0003), AFOSR-MURI Photonic Quantum Matter (Grant No. FA9550-16-1-0323), AFOSR-MURI Quantum Phases of Matter (Grant No. FA9550-14-1-0035), ONR (Grant No. N00014-17-1-2253), the Vannevar-Bush Faculty Fellowship, and the Gordon and Betty Moore Foundation EPiQS Initiative (Grant No. GBMF4306). W. W. H. is supported in part by the Stanford Institute of Theoretical Physics. Numerical simulations involving matrix product states were performed using the TeNPy library [46].

APPENDIX A: DATA ANALYSIS

We determine the contrast $\mathcal{C}$ by a fit $f(y,z) = g(y,z)\cdot[1+\mathcal{C}\cos(Qz+\theta)]/2$ to the two-dimensional phase-contrast images (see Fig. 6). Here, $Q = 2\pi/\lambda$ is the wave vector, θ is a random phase which varies from shot to shot due to small magnetic bias field drifts, and $g(y,z)$ is a two-dimensional envelope function which accounts for the spatial distribution of all atoms $n = n_\uparrow + n_\downarrow$ inside a sphere of radius R such that $g(y,z) = A\sqrt{1-y^2/R^2-z^2/R^2}\cdot H(1-y^2/R^2-z^2/R^2)$ with the Heaviside function $H(r)$. During the evolution time t, the contrast $\mathcal{C}(t)$ decays, and we study the dependence of $c(t) = \mathcal{C}(t)/\mathcal{C}(0)$ on lattice depth V_z, wavelength λ, and anisotropy Δ.

For both longitudinal and transverse spin relaxation, we find the decay curves can be well described by the sum of a decaying part with decay rate γ and a (damped) oscillating part with frequency ω, resulting in a fitting function

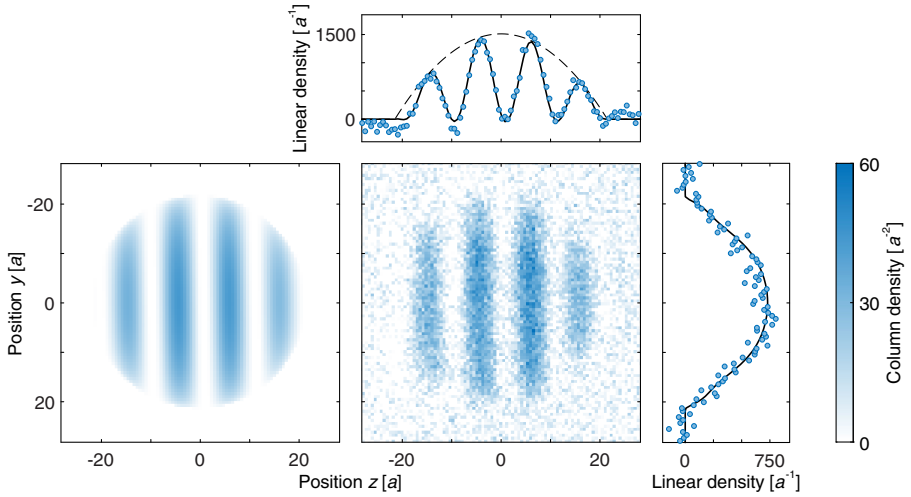

FIG. 6. Contrast measurement. The central image represents raw data and shows the distribution of atoms in the $|\uparrow\rangle$ state. The left image is the two-dimensional fit as described in Appendix A. Every pixel is a local measurement of the column density (number of $|\uparrow\rangle$ atoms per unit area). The image is projected (integrated) along both the horizontal z direction (right) and the vertical y direction (top) from $y, z = -42a$ to $+42a$ to obtain the linear densities (number of $|\uparrow\rangle$ atoms per unit length) for the measured data (points) and the fit (solid line). The dashed line in the y projection shows the (parabolic) envelope function for the spatial density distribution in the cloud. The y and z axes are displayed in units of the lattice spacing $a = 0.532\ \mu$m.

$c(t) = (a_0 + b_0 \cos \omega t)e^{-\gamma t} + c_0$. Here, a_0, b_0, c_0, ω, and γ are fitting parameters. These fits are used for Fig. 2(b) (purple), in Fig. 2(d) (blue), and for Fig. 2(e) (purple and blue). Special fitting procedures are used for the XX model and for the beat note due to the effective magnetic field.

1. XX model

The decay curves $c(t)$ for the transverse spin helix [Fig. 2(a)] clearly show a slower decay rate for larger values of Q. We can use the fitting function described above, with the only difference of adding the constant offset c_0 in quadrature $c(t) = \sqrt{[(a_0 + b_0 \cos \omega t)e^{-\gamma t}]^2 + c_0^2}$ [Fig. 2(a)] to reflect that the offset c_0 arises due to an experimental detection noise floor at the 10^{-2} level. The actual physical contrast does decay to zero $c(t) \to 0$. Remarkably, the fitted oscillation periods [e.g., $T = 11.6(4)\hbar/J_{xy}$ at $\lambda = 10.4a$] agree fairly well with the energy splitting $J_{xy}/2$ for the two-spin Heisenberg model [Fig. 2(c)], which implies an oscillation period of $T = 4\pi\hbar/J_{xy} \approx 12.57\hbar/J_{xy}$. With this fit function, the slower decay for large wave vectors Q shows up mainly in the oscillation frequency ω and not in the decay rate γ. For a simpler characterization of the decay, we obtain the initial decay rate by fitting a linear slope $c(t) = c_0(1 - \gamma t)$ to the initial decay in the range $c(t) \leq 0.4$. Results of such fits are shown in Fig. 2(b) (orange).

2. XXX model

a. Longitudinal spin relaxation [Fig. 2(e), purple]

As in our previous work [32] on spin transport, we use the fitting function $c(t) = (a_0 + b_0 \cos \omega t)e^{-\gamma t} + c_0$.

b. Transverse spin relaxation with spin echo [Figs. 2(d) and 2(e), blue]

The same fitting function yields oscillation frequencies ω and oscillating fractions $b_0/(a_0 + b_0)$ which agree fairly well with the longitudinal case, especially at large wave vectors Q, but with much larger error bars at small wave vectors Q, because the decay rate γ is much faster than the oscillations. For this reason, we constrain both parameters ω and $b_0/(a_0 + b_0)$ to the values obtained in the longitudinal case.

c. Transverse spin relaxation without spin echo [Figs. 2(d) and 2(e), orange; Fig. 3]

A beat note between the inner part and outer part of the cloud is visible (Fig. 3), due to the difference in effective magnetic fields. To determine the beat frequency Ω, we generalize the fitting function to the sum of two parts which interfere: $|c_1(t)e^{i\Omega t} + c_2(t)| = \sqrt{c_1(t)^2 + 2c_1(t)c_2(t)\cos(\Omega t) + c_2(t)^2}$. Here, $c_1(t) = (a_0 + b_0 \cos \omega t)e^{-\gamma t}$ is the contrast of the atoms in the inner part of the cloud, and $c_2(t) = c_2$ is the contrast of the isolated atoms in the outer part which preserve the contrast for a long time. We can neglect the background c_0 due to the detection noise. In $c_1(t)$, we again constrain the two parameters ω and $b_0/(a_0 + b_0)$ to the values obtained for longitudinal spin relaxation.

APPENDIX B: SPECTROSCOPIC OBSERVATION OF THE EFFECTIVE MAGNETIC FIELD

A spatially uniform effective magnetic field can always be transformed away in a suitable rotating frame. However, even then, it can still be observed as a shift of the spin-flip resonance. We rotate the spins via an adiabatic frequency

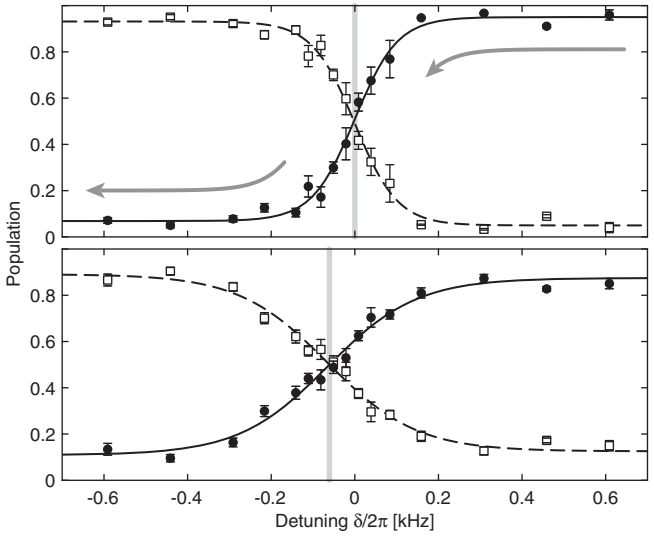

FIG. 7. Spectroscopic observation of the effective magnetic field h_z as a shift in the spin-flip frequency for $h_z < 0$ (bottom) compared to $h_z \approx 0$ (top). Shown is the fraction of atoms in each state as a function of the final detuning δ of a 22-ms sweep of the rf frequency, starting at $\delta = +30$ kHz with all atoms in the $|\uparrow\rangle$ state (closed circles) and no atoms in the $|\downarrow\rangle$ state (open squares). The detuning is relative to the single-particle transition frequency. The power of the rf drive is also ramped to zero after the frequency sweep to make the transition sharper. A nonzero detuning δ for equal spin populations compensates for the effective magnetic field h_z which shifts the curves for a lattice depth of $11E_R$ (bottom) compared to $35E_R$ (top) where $h_z \approx 0$. For the sweep experiment, we choose the second-lowest (closed circles) and third-lowest (open squares) hyperfine states of ^{7}Li due to the smaller sensitivity to external magnetic fields (originating from a smaller differential magnetic moment). At 1025 G, the scattering lengths are approximately $a_{\uparrow\uparrow} \approx a_{\uparrow\downarrow} \approx -50a_0$ and $a_{\downarrow\downarrow} \approx +350a_0$, leading to an estimate for an effective magnetic field of $h_z \approx -1.14J_{xy} \sim h \times (-100\ \text{Hz})$, which is consistent with our observation.

sweep, where the detuning corresponds to an external B_z field (in the rotating frame) and the Rabi frequency to a B_x field, realizing a Heisenberg model with magnetic fields. Starting from a fully polarized state with all atoms in the $|\downarrow\rangle$ state and large detuning of the rf, we reduce the B_z field adiabatically and observe the spin imbalance. The spins are balanced when the detuning compensates for the effective magnetic field created by superexchange. With this method, we can observe the effective field for different lattice depths (Fig. 7).

APPENDIX C: SEMICLASSICAL ANALYSIS AND SHORT-TIME EXPANSION OF SPIN DYNAMICS

1. The classical transverse spin helix with any wave vector Q does not evolve for any anisotropy Δ

We show here that, in the classical limit, the transverse spin helix with any wave vector Q does not evolve under the XXZ Hamiltonian (assuming the effective magnetic field is uniform), for any isotropy Δ. The classical limit is reached by taking the spin-quantum number $S \to \infty$ or by treating the spins as classical vectors $\vec{S}_i = (S_i^x, S_i^y, S_i^z)$ of arbitrary length $S = |\vec{S}_i|$, which we set to $1/2$ for comparison to the quantum spin system.

We start with the system initialized at $t = 0$ in the helix state $S_i^{\pm}(0) = Se^{\pm i(Qz_i+\theta)}, S_i^z(0) = 0$, and we untwist the helix by using the rotation

$$\begin{pmatrix} S_i^x \\ S_i^y \\ S_i^z \end{pmatrix} = \begin{pmatrix} -\sin(Qz_i) & 0 & \cos(Qz_i) \\ \cos(Qz_i) & 0 & \sin(Qz_i) \\ 0 & 1 & 0 \end{pmatrix} \begin{pmatrix} T_i^x \\ T_i^y \\ T_i^z \end{pmatrix} \tag{C1}$$

(we ignore the phase θ for simplicity), which gives $\vec{S}_i \mapsto \vec{T}_i$ with $T_i^{\pm}(0) = 0, T_i^z(0) = S$. The Hamiltonian Eq. (1) (with $h_z = 0$) then transforms as

$$\begin{aligned} H \mapsto H(Q) = J_{xy}\sum_i [&\cos(Qa)(T_i^x T_{i+1}^x + T_i^z T_{i+1}^z) \\ &+ \sin(Qa)(T_i^z T_{i+1}^x - T_i^x T_{i+1}^z)] \\ &+ J_z \sum_i T_i^y T_{i+1}^y. \end{aligned} \tag{C2}$$

The Landau-Lifshitz (LL) equations of motion for classical spins read $\partial_t \vec{T}_i = \partial_{\vec{T}_i} H(Q) \times \vec{T}_i$. Upon changing variables to $T_i^{\pm} = T_i^x \pm iT_i^y$, we have

$$\begin{aligned} \dot{T_i^+} = \frac{1}{2} i\{&J_z(T_{i-1}^- + T_{i+1}^- - T_{i-1}^+ - T_{i+1}^+)T_i^z \\ &+ J_{xy}[\sin(Qa)T_i^+(T_{i-1}^- - T_{i+1}^- + T_{i-1}^+ - T_{i+1}^+) \\ &+ 2T_i^z(T_{i-1}^z - T_{i+1}^z)] \\ &+ \cos(Qa)[-(T_{i-1}^- + T_{i+1}^- + T_{i-1}^+ + T_{i+1}^+)T_i^z \\ &+ 2T_i^+(T_{i-1}^z + T_{i+1}^z)]\}, \end{aligned} \tag{C3}$$

$$\dot{T_i^-} = \dot{T_i^{+*}}, \tag{C4}$$

$$\begin{aligned} \dot{T_i^z} = -\frac{1}{4} i\{&J_z(T_i^- + T_i^+)(T_{i-1}^- + T_{i+1}^- - T_{i-1}^+ - T_{i+1}^+) \\ &- J_{xy}(T_i^- - T_i^+)[\cos(Qa)(T_{i-1}^- + T_{i+1}^- + T_{i-1}^+ + T_{i+1}^+) \\ &+ 2\sin(Qa)(-T_{i-1}^z + T_{i+1}^z)]\}, \end{aligned} \tag{C5}$$

and it is straightforward to verify that $T_i^{\pm}(t) = 0, T_i^z(t) = S$ is a solution to the LL equations, as claimed.

2. Stability of the classical spin-helix state: Dispersion relation of fluctuations

To understand the stability of the classical spin-helix states, we linearize the equations of motion about the classical solution and consider fluctuations. Now, T_i^z obeys

the constraint $T_i^z = \sqrt{S^2 - T_i^+ T_i^-}$, so fluctuations about the classical solution simply entail

$$T_i^\pm(t) = \bar{T}_i^\pm(t) + \delta T_i^\pm(t) + \mathcal{O}((\delta T)^2) = \delta T_i^\pm(t) + \mathcal{O}((\delta T)^2), \tag{C6}$$

$$T_i^z(t) = S + \mathcal{O}((\delta T)^2). \tag{C7}$$

Therefore, we get

$$\begin{aligned}\delta T_i^\pm = \frac{iS}{2}[&J_z(\delta T_{i-1}^- + \delta T_{i+1}^- - \delta T_{i-1}^+ - \delta T_{i+1}^+) \\ &\mp \cos(Qa) J_{xy}(\delta T_{i-1}^- + \delta T_{i+1}^- + \delta T_{i-1}^+ \\ &+ \delta T_{i+1}^+ - 4\delta T_i^\pm)].\end{aligned} \tag{C8}$$

We now expand in Fourier modes $\delta T_i^\pm = \sum_k \delta T_k^\pm e^{i(kz_i + \omega_k t)}$ with momentum k and dispersion ω_k. This reduces to an eigenvalue problem

$$\omega_k \begin{pmatrix} \delta T_k^+ \\ \delta T_k^- \end{pmatrix} = S J_{xy} \begin{pmatrix} -[-2+\cos(ka)]\cos(Qa) - \Delta\cos(ka) & \cos(ka)[-\cos(Qa)+\Delta] \\ \cos(ka)[\cos(Qa)-\Delta] & [-2+\cos(ka)]\cos(Qa) + \Delta\cos(ka) \end{pmatrix} \begin{pmatrix} \delta T_k^+ \\ \delta T_k^- \end{pmatrix} \tag{C9}$$

with solution

$$\omega_k = \pm 2\sqrt{2} J_{xy} S \sqrt{\cos(Qa)[-\Delta\cos(ka) + \cos(Qa)]\sin^2(ka/2)}. \tag{C10}$$

Reducing to $\Delta = 0$ reproduces the expression quoted in the main text for the XX model in Sec. III A. Note that we could have equivalently obtained the same dispersion relations by performing a spin-wave analysis, upon mapping the spins to Holstein-Primakoff bosons (in a large S expansion) and performing a Bogoliubov transformation to diagonalize the Hamiltonian in second order.

3. Short-time expansion of quantum dynamics

Owing to the factorizable nature of the initial spin-helix state, we can analytically derive the short-time quantum dynamics of the state without passing into a semiclassical limit as done before. The basic object is the Taylor expansion of a spin operator (in the transverse direction):

$$\langle S_i^+(t)\rangle = \langle S_i^+(0)\rangle + \langle \partial_t S_i^+(0)\rangle t + \frac{1}{2}\langle \partial_t^2 S_i^+(0)\rangle t^2 + \cdots, \tag{C11}$$

where $\langle\cdot\rangle$ is the expectation value in the spin state $|\psi(Q)\rangle = e^{-i\sum_i S_i^z Q z_i}|+++\cdots\rangle$, where $S_i^x|+\rangle_i = S|+\rangle_i$, and

$$\langle \partial_t S_i^+(0)\rangle = i\langle [H, S_i^+]\rangle, \tag{C12}$$

$$\langle \partial_t^2 S_i^+(0)\rangle = -\langle [H,[H,S_i^+]]\rangle. \tag{C13}$$

Since the Hamiltonian is a sum of strictly local terms and S_i^+ is an on-site term, the expressions in the commutators are comprised of only finite-range terms with support centered around site i. Using that the state factorizes into a product state, we can easily evaluate the expression for these terms. We find for general spin S

$$i\langle [H, S_i^+]\rangle = 0, \tag{C14}$$

$$-\langle [H,[H,S_i^+]]\rangle = -S^2 e^{iQz_i}[J_z - J_{xy}\cos(Qa)]^2. \tag{C15}$$

(The vanishing of the term linear in t follows from time-reversal symmetry.) Therefore,

$$\langle S_i^+(t)\rangle = S e^{iQz_i} - \frac{1}{2} S^2 e^{iQz_i}[J_z - J_{xy}\cos(Qa)]^2 t^2 + \cdots. \tag{C16}$$

Extracting the Fourier component with wave vector Q gives the normalized contrast

$$c(t) = 1 - \frac{1}{2} S[J_z - J_{xy}\cos(Qa)]^2 t^2 + \cdots. \tag{C17}$$

A characteristic energy rate γ for the initial quadratic decay can, therefore, be defined as $c(t) = 1 - \gamma^2 t^2 + \cdots$, yielding

$$\gamma := \sqrt{\frac{S}{2}} |J_{xy}[\Delta - \cos(Qa)]|. \tag{C18}$$

Focusing now on $\Delta = 0$ and $S = 1/2$, this shows that a helix of wave vector Q decays with a rate going as $\gamma \propto |\cos(Qa)|$. For $\Delta = 1$, we recover that $\gamma \propto Q^2$ in the limit of $Q \ll 1/a$ (when the wavelength λ is large compared to the lattice spacing a). More generally, for arbitrary anisotropy Δ, there is a critical wave vector $(Q_c a) = \arccos(\Delta)$ where decay is expected to be very

slow; seeing such a dependence in experiments would be interesting. This prediction is actually in line with that the spin helix with wave vector $(Q_c a) = \arccos(\Delta)$ can be proven to be an *exact* eigenstate of the XXZ Hamiltonian with anisotropy Δ with appropriate boundary conditions, as shown in Refs. [38,39].

APPENDIX D: NUMERICAL SIMULATION DETAILS

Here, we present general details on the numerical simulations performed. Unless otherwise specified, we employ the time-evolving block decimation algorithm on matrix product states defined on 1D chains of length $L = 40a$, with large enough bond dimension to ensure convergence of local observables to a tolerance 10^{-4}, via the TeNPy library [46].

In the absence of holes, we simulate the Heisenberg model (1), with the initial state the spin helix with wave vector Q, which reads locally $|\psi_i(Q)\rangle = e^{i(Qz_i+\theta)S_i^z}|+\rangle_i$, where $S_i^x|+\rangle_i = |+\rangle_i = (1/\sqrt{2})(|\uparrow\rangle_i + |\downarrow\rangle_i)$. Here, θ is the global initial phase of the spin helix, which varies from shot to shot in the experiment due to small magnetic field bias drifts (Appendix A). We measure $\langle S_i^x(t)\rangle$ and fit for each time slice a sine function in space with wave vector Q (allowing its phase to be an independent parameter); the amplitude of the sinusoidal modulation is the numerically determined contrast $c(t)$ normalized to unity at $t = 0$. We also average $c(t)$ over $\theta = 0, \pi/2$ to account for the fact that the global phase of the initial state in the experiments shifts from measurement to measurement (we find that averaging over these two values suffices to reproduce the full averaging over θ; also see the methods section in Ref. [32]).

In the presence of holes, we simulate the bosonic $\tilde{t}$-J model [Eq. (F1)]. We assume holes occur independently on each site with probability p. In order to perform ensemble averaging over the different hole positions of the initial state, we employ the following computational trick. Let the on-site Hilbert space be spanned by the states $|0\rangle$, $|\uparrow\rangle_i \coloneqq a_{i\uparrow}^\dagger|0\rangle$, and $|\downarrow\rangle_i \coloneqq a_{i\downarrow}^\dagger|0\rangle$. We define a pure state on each site as

$$|\Psi_i(Q)\rangle = e^{i\varphi_i}\sqrt{1-p}|\psi_i(Q)\rangle + \sqrt{p}|0\rangle_i, \quad \text{(D1)}$$

where φ_i is some phase with value in $[0, 2\pi)$. Clearly, in the limit $p \to 0$, the state $|\Psi(Q)\rangle \coloneqq \prod_i |\Psi_i(Q)\rangle$ reduces to the pure-spin helix (i.e., without holes) with wave vector Q. Consider now the outer product of $|\Psi_i(Q)\rangle$ with itself when $p \neq 0$:

$$\rho_i = (1-p)|\psi_i(Q)\rangle\langle\psi_i(Q)| + e^{i\varphi_i}\sqrt{1-p}|\psi_i(Q)\rangle\langle 0|_i + \text{H.c.} + p|0\rangle_i\langle 0|_i. \quad \text{(D2)}$$

If we now average φ over the interval $[0, 2\pi)$ uniformly, the ensemble-averaged reduced density matrix is

$$\bar{\rho}_i = \frac{1}{2\pi}\int_0^{2\pi} d\varphi\ \rho_i = (1-p)|\psi_i(Q)\rangle\langle\psi_i(Q)| + p|0\rangle_i\langle 0|_i. \quad \text{(D3)}$$

This reproduces the situation where holes occur locally and independently on each site i with probability p.

In our simulations, we choose a random set of phase angles $(\varphi_1, \ldots, \varphi_N) \in [0, 2\pi)^N$ and time evolve the globally pure state $\prod_i |\Psi_i(Q)\rangle$ under the $\tilde{t}$-J Hamiltonian. We repeat the simulation with different sets of phase angles sampled randomly uniformly in $[0, 2\pi)^N$ and then average the extracted contrast.

We find that, in practice, there are remarkably only very small variations between different choices of phase angles [i.e., a given random choice of $\prod_i |\Psi_i(Q)\rangle$ is a typical configuration], allowing us to perform the ensemble average with relatively few repetitions (at most 50 runs for each Q and global phase θ).

APPENDIX E: NUMERICAL SIMULATION RESULTS

1. XX model

For the XX model, we utilize parameters $\Delta = 0$ and $h_z = 1.43J_{xy}$ (thus, simulating the experimental conditions at $V_z = 11E_R$), as well as $\tilde{t} = 4.11J_{xy}$, $J_{\uparrow\uparrow}/J_{\uparrow\downarrow} = -0.32$, and $J_{\downarrow\downarrow}/J_{\uparrow\downarrow} = 1.15$. Here, $J_{\sigma\sigma'} \coloneqq -4\tilde{t}^2/U_{\sigma\sigma'}$.

Figure 8 shows decay curves for $p = 0$, 0.05, and 0.1. The experimental decay rates $\gamma = 1/\tau$ [in Fig. 2(b)] are obtained from a linear fit $c(t) = c_0(1 - t/\tau)$ to the initial decay [$c(t) \leq 0.4$]. We use an equivalent procedure for the theoretical data and determine the time τ' where the numerical simulations show a contrast of $c(\tau') = 0.4$, which we then convert to the theoretical decay rate $\tau = (5/3)\tau'$. As shown in Fig. 2(b), the numerical data verifies the analytically predicted $\cos(Qa)$ dependence of the decay rate. This scaling starts to break down as $Q \to \pi/(2a)$, because higher-order terms in the expansion (either semiclassical or short-time) become important. Inclusion of holes washes out the $\cos(Qa)$ dependence.

2. XXX model

For the XXX model, we utilize parameters $\Delta = 1$ and $h_z = 0.80J_{xy}$ (thus, simulating the experimental conditions at $V_z = 11E_R$), as well as $\tilde{t} = 6.13J_{xy}$, $J_{\uparrow\uparrow}/J_{\uparrow\downarrow} = 0.61$, and $J_{\downarrow\downarrow}/J_{\uparrow\downarrow} = 1.40$.

Figures 9(a) and 9(b) show the results for a simulation involving 10% holes, i.e., $p = 0.1$. We fit the data between $c(t) = 0.9$ and 0.15 with a straight line (dashed) and obtain a decay rate defined as twice the slope of the fit (this factor is chosen because the slope of an exponential function at half decay is reduced by a factor of 2). Because of the nonexponential nature of the decay curves, for both

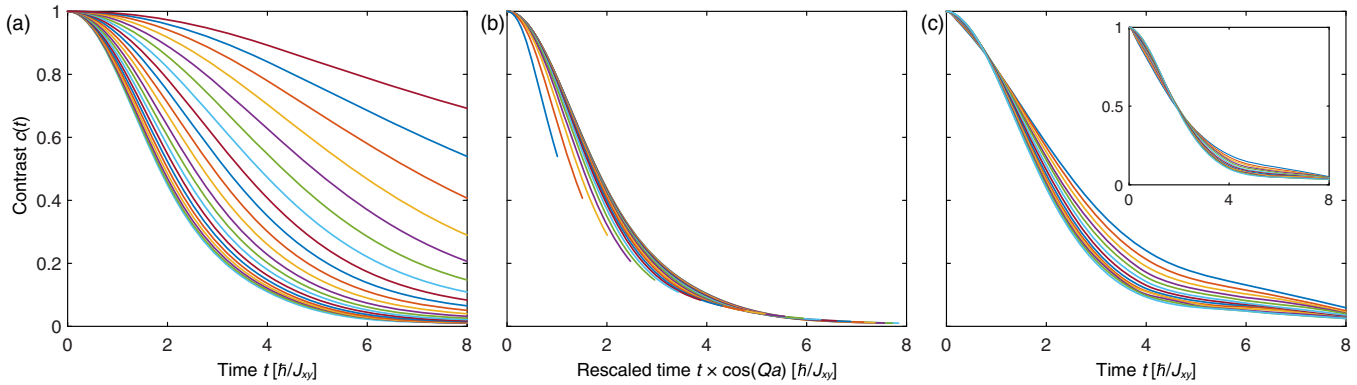

FIG. 8. Transverse spin-helix decay for the XX model obtained from numerical simulations, with hole probability $p = 0$ (a),(b), $p = 0.05$ (c), and $p = 0.1$ [(c), inset] with $h_z = 0$ (a),(b) and $h_z = 1.43J_{xy}$ (c) as in the experiment. The wavelengths in (a) are (from bottom to top) $\lambda = 31.3a$, $23.5a$, $18.8a$, $15.7a$, $13.4a$, $11.7a$, $10.4a$, $9.4a$, $8.5a$, $7.8a$, $7.2a$, $6.7a$, $6.3a$, $5.9a$, $5.6a$, $5.3a$, $5.0a$, $4.8a$, $4.6a$, $4.4a$, and $4.0a$. The decay curves for pure spin dynamics (a) show a wave-vector dependence of decay rates of the form $\gamma \propto \cos(Qa)$. Using rescaled time $t\cos(Qa)$, all decay curves collapse almost perfectly for wavelengths $\lambda \geq 6.3a$, which covers the range studied in the experiment. The presence of holes washes out the $\cos(Qa)$ dependence (c), shown here for $\lambda \geq 6.3a$ and $p = 0.05$. At sufficiently high hole probability, e.g., $p = 0.1$ [(c), inset], the wave-vector dependence vanishes almost completely.

numerical simulations and experimental data, there is some arbitrariness in choosing "effective" decay rates which, depending on the parameterization, could differ by up to 50%. By further fitting the decay rates for the six smallest values of Q values to the form $\gamma(Q) = DQ^2 + \gamma_0$ (in order to focus on the limiting $Q \to 0$ behavior), we obtain a Q-independent decay rate $\gamma_0 = 0.019J_{xy}/\hbar$ and a diffusion constant $D = 0.16a^2/(\hbar/J_{xy})$.

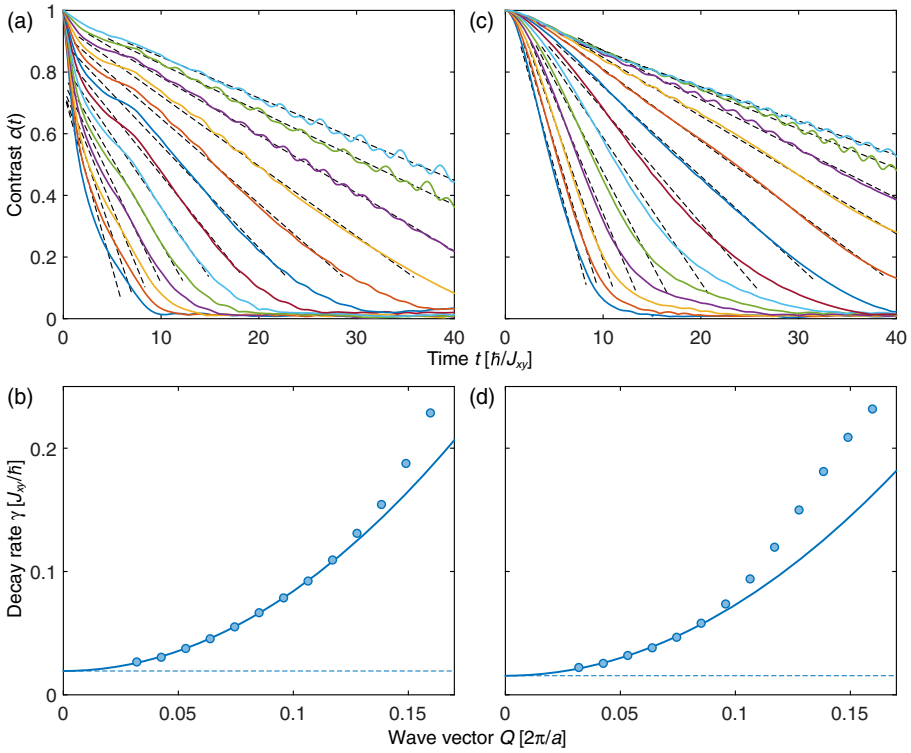

FIG. 9. Spin relaxation for the XXZ model. (a),(b) Isotropic model $\Delta = 1$ with finite hole concentration ($p = 0.1$). (c),(d) Slightly anisotropic $\Delta = 0.93$ with no holes ($p = 0$). The colored solid lines in (a) and (c) are decay curves $c(t)$ for different wavelengths $\lambda = 31.3a$, $23.5a$, $18.8a$, $15.7a$, $13.4a$, $11.7a$, $10.4a$, $9.4a$, $8.5a$, $7.8a$, $7.2a$, $6.7a$, and $6.3a$ (from top to bottom). The dotted lines are linear fits to determine decay rates, which are shown in (b) and (d) with a fit $\gamma = DQ^2 + \gamma_0$ (solid line).

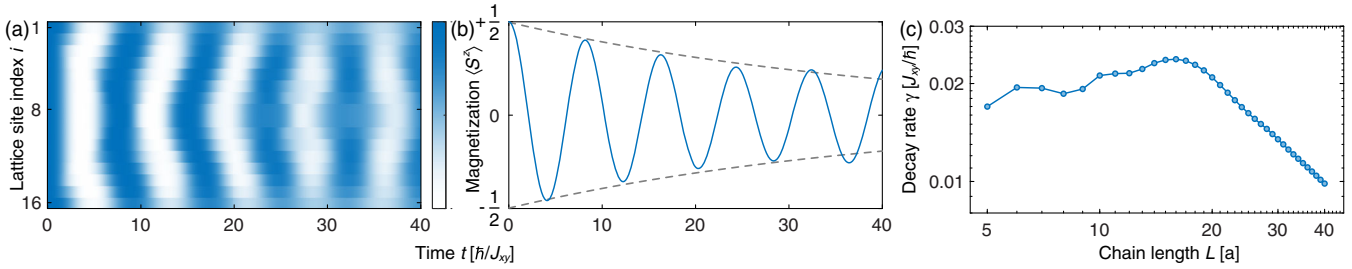

FIG. 10. Dephasing from the edges of the chains. (a),(b) Dynamics of an S_x-polarized ($Q = 0$) state for an $L = 16a$ finite chain, with anisotropy $\Delta = 1$ and $h_z = 0.8J_{xy}$ reflecting the parameters of the experiment. (a) shows how the initially homogeneous phase of the locally measured transverse spin $\langle S_i^x(t)\rangle$ gets distorted at the edges and how this perturbation propagates through the chain, leading to a loss of overall contrast of the total transverse magnetization $\sum_i \langle S_i^x(t)\rangle$ (b). A fit (dashed lines) to $\cos(\omega t + \phi)e^{-\gamma t}/2$ determines the decay rate γ, which is shown as a function of system size L in (c). A log-log plot shows the scaling $\gamma \propto L^{-1}$ for large L.

3. Near-isotropic *XXZ* model

We also investigate how a small deviation from the isotropic point affects dynamics. One reason is that our experimental data for the isotropic model is actually not taken exactly at the isotropic point but at $\Delta = 0.93 \pm 0.05$. In the two-site model, the triplet splitting of $J_{xy}(1-\Delta)/2$ becomes $0.035J_{xy}/\hbar$, but the full simulation presented here shows that the effect is smaller.

We consider $\Delta = 0.93$ and $h_z = 0.89J_{xy}$ (thus, simulating the experimental conditions at $V_z = 11E_R$), as well as $\tilde{t} = 6.15J_{xy}$, $J_{\uparrow\uparrow}/J_{\uparrow\downarrow} = 0.53$, and $J_{\downarrow\downarrow}/J_{\uparrow\downarrow} = 1.41$. Figures 9(c) and 9(d) show the results for a simulation in the absence of holes. We use the same method as for the *XXX* model to determine decay rates from linear fits. We obtain a Q-independent decay rate $\gamma_0 = 0.015J_{xy}/\hbar$ and a diffusion constant $D = 0.15a^2/(\hbar/J_{xy})$.

4. Dephasing from edge effects

We also use numerical simulations to study how the inhomogeneity of the effective magnetic field at the ends of finite chains leads to dephasing for transverse spin components. We concentrate on the $Q \to 0$ limit, i.e., a state uniformly polarized in the S_x direction, with anisotropy $\Delta = 1$.

If the effective magnetic field is globally uniform, the transverse magnetization $\sum_i \langle S_i^x(t)\rangle$ just oscillates in time without decaying. However, the fact that the edges of the chain feel an effective magnetic field strength which is half that of the bulk causes dephasing of spins at the edges. This disturbance, in turn, propagates into the bulk [see Fig. 10(a)], so that the transverse magnetization decays in time [see Fig. 10(b)]. For long chains, the decay rate decreases as a function of length L, as the bulk dominates the edges. This trend starts only for chains with $L > 16a$. For smaller L, the trend is reversed due to few-body dynamics.

We also explore the effect of the effective magnetic field in the *XX* model. Comparison of simulations of the pure spin model with and without an effective magnetic field of $h_z = 1.43J_{xy}$ shows that the edge effect for chains of length $L = 40a$ give rise to a Q-independent decay rate of $0.04\hbar/J_{xy}$, which amounts to shifting the black curve in Fig. 2(b) (for $h_z = 0$) vertically.

APPENDIX F: DERIVATION OF THE BOSONIC $\tilde{t}$-J MODEL

We derive here the bosonic $\tilde{t}$-J model

$$H_{\tilde{t}-J} = \sum_{\langle ij\rangle}\left[J_{xy}(S_i^xS_j^x + S_i^yS_j^y) + J_zS_i^zS_j^z - \frac{h_z}{2}[S_i^z(n_{j\uparrow}+n_{j\downarrow}) + (n_{i\uparrow}+n_{i\downarrow})S_j^z] + c(n_{i\uparrow}+n_{i\downarrow})(n_{j\uparrow}+n_{j\downarrow})\right]$$
$$- \sum_{\langle ij\rangle,\sigma}\tilde{t}\,a_{i\sigma}^\dagger a_{j\sigma} + \text{H.c.} - \sum_{\langle ijk\rangle,\sigma}\left[\frac{\tilde{t}^2}{U_{\uparrow\downarrow}}a_{i\sigma}^\dagger n_{j\bar{\sigma}}a_{k\sigma} + \frac{\tilde{t}^2}{U_{\uparrow\downarrow}}a_{i\bar{\sigma}}^\dagger S_j^\sigma a_{k\sigma} + \frac{2\tilde{t}^2}{U_{\sigma\sigma}}a_{i\sigma}^\dagger n_{j\sigma}a_{k\sigma}\right] + \text{H.c.} \quad \text{(F1)}$$

quoted in the main text. Here, spin $\sigma = \uparrow, \downarrow$, and $a_{i\sigma}$ and $a_{i\sigma}^\dagger$ are bosonic lowering and raising operators, respectively, at site i, such that $S_i^\uparrow \equiv S_i^+ := a_{i\uparrow}^\dagger a_{i\downarrow}$, $S_i^\downarrow \equiv S_i^- = (S_i^+)^\dagger$, and $S_i^x = \frac{1}{2}(S_i^+ + S_i^-)$, $S^y = \frac{1}{2i}(S_i^+ - S_i^-)$, $S^z = \frac{1}{2}(n_{i\uparrow} - n_{i\downarrow})$ form a representation of the Pauli algebra, upon restricting the on-site Hilbert space to be spanned by three states: an occupancy of a single boson (either spin $|\uparrow\rangle$ or $|\downarrow\rangle$) or no boson (hole). Also, $c = -(\tilde{t}^2/U_{\uparrow\uparrow} + \tilde{t}^2/U_{\downarrow\downarrow} + \tilde{t}^2/U_{\uparrow\downarrow})$.

The above Hamiltonian illustrates that the previously identified effective magnetic field term $\sum_{\langle ij\rangle}(h_z/2)(S_i^z + S_j^z)$ in fact stems from a direct *interaction* term describing

magnon-density coupling $S_i^z(n_{j\uparrow}+n_{j\downarrow})+(i\leftrightarrow j)$, the latter of which reduces to the former upon taking the limit of no holes, i.e., $(n_{i\uparrow}+n_{i\downarrow})=1$ for every site i. The terms on the lower line represent dynamics of holes in different flavors: bare tunneling, density-assisted tunneling, and spin-flip-assisted tunneling, which are additional magnon-hole couplings. Note that they arise at the same order in perturbation theory (in $\tilde{t}/U_{\sigma\sigma'}$) as the pure spin couplings and, thus, in principle, cannot be neglected, although they *are* suppressed by the presence of a small hole probability p. By inspecting the expressions of J_z, h_z, and these extra terms as a function of $U_{\uparrow\uparrow}$, $U_{\uparrow\downarrow}$, and $U_{\downarrow\downarrow}$, we see that at $\Delta=1$ (isotropic spin couplings) a nonzero h_z is a *necessary* and *sufficient* condition for the $\tilde{t}$-J model to break spin rotational symmetry. (Having spin rotational symmetry requires all on-site interaction energies to be equal $U_{\uparrow\uparrow}=U_{\uparrow\downarrow}=U_{\downarrow\downarrow}$.) This justifies our identification of the effective magnetic field as the agent giving rise to differences in dynamics between the transverse and the longitudinal spin helix.

To derive the bosonic $\tilde{t}$-J model, the starting point is the Bose-Hubbard Hamiltonian describing cold atoms moving in a deep optical lattice (so that they are confined to the lowest Bloch band):

$$H=-\sum_{\langle ij\rangle,\sigma}\tilde{t}(a_{i\sigma}^\dagger a_{j\sigma}+\text{H.c.})+\frac{1}{2}\sum_{i,\sigma}U_{\sigma\sigma}n_{i\sigma}(n_{i\sigma}-1)+U_{\uparrow\downarrow}\sum_i n_{i\uparrow}n_{i\downarrow}. \tag{F2}$$

We assume two components $\sigma=\uparrow,\downarrow$ and $U_{\sigma\sigma'}\gg\tilde{t}$, such that there are at most singly occupied sites. We derive the effective model in this limit. We do not assume $U_{\uparrow\uparrow}$, $U_{\uparrow\downarrow}$, and $U_{\downarrow\downarrow}$ are necessarily equal between themselves.

We employ the expansion detailed in Ref. [47], where it is shown how having multiple emergent $U(1)$ charges emerge in an effective Hamiltonian. The general setup is as such: Let $\Gamma_1,\ldots,\Gamma_m$ be m mutually commuting operators with integer eigenvalue spacings, and consider the Hamiltonian

$$H=\vec{\omega}\cdot\vec{\Gamma}+V, \tag{F3}$$

where V need not commute with Γ_i. In the limit of large $|\vec{\omega}|$, we can derive an effective Hamiltonian

$$H_{\text{eff}}=\vec{\omega}\cdot\vec{\Gamma}+H_0'+\frac{1}{2}\sum_{\vec{n}\neq\vec{0}}\frac{[H_{\vec{n}}',H_{-\vec{n}}']}{\vec{n}\cdot\vec{\omega}}+\cdots \tag{F4}$$

(this turns out to be the so-called van Vleck expansion). The effective Hamiltonian has emergent symmetries $[H_{\text{eff}},\Gamma_i]=0$; i.e., the Hamiltonian is symmetric with respect to the m $U(1)$ charges Γ_i. Here, $H_{\vec{n}}'$ is the $\vec{n}$th Fourier mode of the "interaction" Hamiltonian defined on the m-torus $\mathbb{T}^m$:

$$H'(\vec{\theta})=U_0^\dagger(\vec{\theta})VU_0(\vec{\theta}), \tag{F5}$$

$$U_0(\vec{\theta})=e^{-i\vec{\theta}\cdot\vec{\Gamma}}, \tag{F6}$$

$$H_{\vec{n}}'=\frac{1}{(2\pi)^m}\int_{\mathbb{T}^m}d^m\theta\; e^{-i\vec{n}\cdot\vec{\theta}}H'(\vec{\theta}). \tag{F7}$$

Applying this formalism to the Bose-Hubbard model, we note that interactions there consist of three kinds:

$$U_{\downarrow\downarrow}\Gamma_1;\qquad \Gamma_1=\sum_i\frac{1}{2}n_{i\downarrow}(n_{i\downarrow}-1), \tag{F8}$$

$$U_{\uparrow\uparrow}\Gamma_2;\qquad \Gamma_2=\sum_i\frac{1}{2}n_{i\uparrow}(n_{i\uparrow}-1), \tag{F9}$$

$$U_{\uparrow\downarrow}\Gamma_3;\qquad \Gamma_3=\sum_i n_{i\uparrow}n_{i\downarrow} \tag{F10}$$

and that Γ_i have integer eigenvalues and mutually commute. We, therefore, identify $\omega_1=U_{\downarrow\downarrow}$, $\omega_2=U_{\uparrow\uparrow}$, and $\omega_3=U_{\uparrow\downarrow}$. We define

$$U_0(\vec{\theta})\coloneqq\exp(-i\vec{\theta}\cdot\vec{\Gamma}), \tag{F11}$$

which gives us

$$H'(\vec{\theta})\coloneqq U_0(\vec{\theta})^\dagger\sum_{\langle ij\rangle,\sigma}\tilde{t}(a_{i\sigma}^\dagger a_{j\sigma}+\text{H.c.})U_0(\vec{\theta}). \tag{F12}$$

We have

$$\begin{aligned}e^{i\theta_3\Gamma_3}a_{i\uparrow}^\dagger e^{-i\theta_3\Gamma_3}&=a_{i\uparrow}^\dagger+(i\theta_3)[n_{i\uparrow}n_{i\downarrow},a_{i\uparrow}^\dagger]+\frac{(i\theta_3)^2}{2!}\\&\quad\times[n_{i\uparrow}n_{i\downarrow},[n_{i\uparrow}n_{i\downarrow},a_{i\uparrow}^\dagger]]+\cdots\\&=a_{i\uparrow}^\dagger+(i\theta_3)a_{i\uparrow}^\dagger n_{i\downarrow}+\frac{(i\theta_3)^2}{2!}a_{i\uparrow}^\dagger(n_{i\downarrow}^\dagger)^2+\cdots\\&=a_{i\uparrow}^\dagger e^{i\theta_3 n_{i\downarrow}}.\end{aligned} \tag{F13}$$

Therefore,

$$e^{i\theta_3\Gamma_3}a_{i\uparrow}^\dagger e^{-i\theta_3\Gamma_3}=a_{i\uparrow}^\dagger e^{i\theta_3 n_{i\downarrow}}, \tag{F14}$$

$$e^{i\theta_3\Gamma_3}a_{i\uparrow}e^{-i\theta_3\Gamma_3}=a_{i\uparrow}e^{-i\theta_3 n_{i\downarrow}}, \tag{F15}$$

$$e^{i\theta_3\Gamma_3}a_{i\downarrow}^\dagger e^{-i\theta_3\Gamma_3}=a_{i\downarrow}^\dagger e^{i\theta_3 n_{i\uparrow}}, \tag{F16}$$

$$e^{i\theta_3\Gamma_3}a_{i\downarrow}e^{-i\theta_3\Gamma_3}=a_{i\downarrow}e^{-i\theta_3 n_{i\uparrow}}. \tag{F17}$$

Next,

$$e^{i\theta_2\Gamma_2}a_{i\uparrow}^\dagger e^{-i\theta_2\Gamma_2} = a_{i\uparrow}^\dagger + (i\theta_2)\left[\frac{1}{2}n_{i\uparrow}(n_{i\uparrow}-1), a_{i\uparrow}^\dagger\right] + \frac{(i\theta_2)^2}{2!}\left[\frac{1}{2}n_{i\uparrow}(n_{i\uparrow}-1), \left[\frac{1}{2}n_{i\uparrow}(n_{i\uparrow}-1), a_{i\uparrow}^\dagger\right]\right] + \cdots. \tag{F18}$$

A single commutator yields

$$\begin{aligned}\left[\frac{1}{2}n_{i\uparrow}(n_{i\uparrow}-1), a_{i\uparrow}^\dagger\right] &= \frac{1}{2}[n_{i\uparrow}, a_{i\uparrow}^\dagger](n_{i\uparrow}-1) + \frac{1}{2}n_{i\uparrow}[(n_{i\uparrow}-1), a_{i\uparrow}^\dagger] \\ &= \frac{1}{2}a_{i\uparrow}^\dagger(n_{i\uparrow}-1) + \frac{1}{2}n_{i\uparrow}a_{i\uparrow}^\dagger \\ &= a_{i\uparrow}^\dagger n_{i\uparrow}\end{aligned} \tag{F19}$$

so the full expression becomes

$$\begin{aligned}e^{i\theta_2\Gamma_2}a_{i\uparrow}^\dagger e^{-i\theta_2\Gamma_2} &= a_{i\uparrow}^\dagger + (i\theta_2)a_{i\uparrow}^\dagger n_{i\uparrow} + \frac{(i\theta_2)^2}{2!}a_{i\uparrow}^\dagger(n_{i\uparrow})^2 + \cdots \\ &= a_{i\uparrow}^\dagger e^{i\theta_2 n_{i\uparrow}}.\end{aligned} \tag{F20}$$

Similarly, we have

$$e^{i\theta_2\Gamma_2}a_{i\uparrow}e^{-i\theta_2\Gamma_2} = e^{-i\theta_2 n_{i\uparrow}}a_{i\uparrow}. \tag{F21}$$

Therefore, there are four terms in $H'(\vec{\theta})$:

$$U_0(\vec{\theta})^\dagger a_{i\uparrow}^\dagger a_{j\uparrow}U_0(\vec{\theta}) = a_{i\uparrow}^\dagger e^{i(\theta_3 n_{i\downarrow}+\theta_2 n_{i\uparrow})}e^{-i(\theta_3 n_{j\downarrow}+\theta_2 n_{j\uparrow})}a_{j\uparrow}, \tag{F22}$$

$$U_0(\vec{\theta})^\dagger a_{j\uparrow}^\dagger a_{i\uparrow}U_0(\vec{\theta}) = a_{j\uparrow}^\dagger e^{i(\theta_3 n_{j\downarrow}+\theta_2 n_{j\uparrow})}e^{-i(\theta_3 n_{i\downarrow}+\theta_2 n_{i\uparrow})}a_{i\uparrow}, \tag{F23}$$

$$U_0(\vec{\theta})^\dagger a_{i\downarrow}^\dagger a_{j\downarrow}U_0(\vec{\theta}) = a_{i\downarrow}^\dagger e^{i(\theta_3 n_{i\uparrow}+\theta_1 n_{i\downarrow})}e^{-i(\theta_3 n_{j\uparrow}+\theta_1 n_{j\downarrow})}a_{j\downarrow}, \tag{F24}$$

$$U_0(\vec{\theta})^\dagger a_{j\downarrow}^\dagger a_{i\downarrow}U_0(\vec{\theta}) = a_{j\downarrow}^\dagger e^{i(\theta_3 n_{j\uparrow}+\theta_1 n_{j\downarrow})}e^{-i(\theta_3 n_{i\uparrow}+\theta_1 n_{i\downarrow})}a_{i\downarrow}. \tag{F25}$$

Now, the $\vec{n}$th Fourier mode of $H'(\vec{\theta})$ enforces projectors of certain occupation numbers between sites. For example, for the first term and $n_1 = 0$, $n_2 = 0$, $n_3 = 1$, this is

$$a_{i\uparrow}^\dagger \mathbb{P}_{n_{i\downarrow}-n_{j\downarrow}=1}\mathbb{P}_{n_{i\uparrow}-n_{j\uparrow}=0}a_{j\uparrow}. \tag{F26}$$

We evaluate Eq. (F4), and the result is Eq. (F1) (ignoring the constant term $\vec{\omega}\cdot\vec{\Gamma}$).

[1] W. Heisenberg, *Mehrkörperproblem und Resonanz in der Quantenmechanik*, Z. Phys. **38**, 411 (1926).

[2] P. A. M. Dirac, *On the Theory of Quantum Mechanics*, Proc. R. Soc. A **112**, 661 (1926).

[3] J. H. V. Vleck, *The Theory of Electric and Magnetic Susceptibilities*, International Series of Monographs on Physics (Oxford University, New York, 1932).

[4] A. Auerbach, *Interacting Electrons and Quantum Magnetism* (Springer-Verlag, Berlin, 1994).

[5] K. Binder and A. P. Young, *Spin Glasses: Experimental Facts, Theoretical Concepts, and Open Questions*, Rev. Mod. Phys. **58**, 801 (1986).

[6] L. Savary and L. Balents, *Quantum Spin Liquids: A Review*, Rep. Prog. Phys. **80**, 016502 (2017).

[7] R. Vasseur and J. E. Moore, *Nonequilibrium Quantum Dynamics and Transport: From Integrability to Many-Body Localization*, J. Stat. Mech. (2016) 064010.

[8] B. Bertini, F. Heidrich-Meisner, C. Karrasch, T. Prosen, R. Steinigeweg, and M. Žnidarič, *Finite-Temperature Transport in One-Dimensional Quantum Lattice Models*, Rev. Mod. Phys. **93**, 025003 (2021).

[9] M. Ljubotina, M. Žnidarič, and T. Prosen, *Spin Diffusion from an Inhomogeneous Quench in an Integrable System*, Nat. Commun. **8**, 16117 (2017).

[10] S. Gopalakrishnan and R. Vasseur, *Kinetic Theory of Spin Diffusion and Superdiffusion in XXZ Spin Chains*, Phys. Rev. Lett. **122**, 127202 (2019).

[11] E. Ilievski, J. De Nardis, M. Medenjak, and T. Prosen, *Superdiffusion in One-Dimensional Quantum Lattice Models*, Phys. Rev. Lett. **121**, 230602 (2018).

[12] B. Bertini, M. Collura, J. De Nardis, and M. Fagotti, *Transport in Out-of-Equilibrium XXZ Chains: Exact Profiles of Charges and Currents*, Phys. Rev. Lett. **117**, 207201 (2016).

[13] O. A. Castro-Alvaredo, B. Doyon, and T. Yoshimura, *Emergent Hydrodynamics in Integrable Quantum Systems out of Equilibrium*, Phys. Rev. X **6**, 041065 (2016).

[14] M. Babadi, E. Demler, and M. Knap, *Far-from-Equilibrium Field Theory of Many-Body Quantum Spin Systems: Prethermalization and Relaxation of Spin Spiral States in Three Dimensions*, Phys. Rev. X **5**, 041005 (2015).

[15] S. Bhattacharyya, J. F. Rodriguez-Nieva, and E. Demler, *Universal Prethermal Dynamics in Heisenberg Ferromagnets*, Phys. Rev. Lett. **125**, 230601 (2020).

[16] J. F. Rodriguez-Nieva, A. Schuckert, D. Sels, M. Knap, and E. Demler, *Transverse Instability and Universal Decay of Spin Spiral Order in the Heisenberg Model*, arXiv:2011.07058.

[17] J. F. Rodriguez-Nieva, *Turbulent Relaxation after a Quench in the Heisenberg Model*, Phys. Rev. B **104**, L060302 (2021).

[18] C. Gross and I. Bloch, *Quantum Simulations with Ultracold Atoms in Optical Lattices*, Science **357**, 995 (2017).

[19] D. Jaksch, C. Bruder, J. I. Cirac, C. W. Gardiner, and P. Zoller, *Cold Bosonic Atoms in Optical Lattices*, Phys. Rev. Lett. **81**, 3108 (1998).

[20] A. B. Kuklov and B. V. Svistunov, *Counterflow Superfluidity of Two-Species Ultracold Atoms in a Commensurate Optical Lattice*, Phys. Rev. Lett. **90**, 100401 (2003).

[21] L.-M. Duan, E. Demler, and M. D. Lukin, *Controlling Spin Exchange Interactions of Ultracold Atoms in Optical Lattices*, Phys. Rev. Lett. **91**, 090402 (2003).

[22] J. J. García-Ripoll and J. I. Cirac, *Spin Dynamics for Bosons in an Optical Lattice*, New J. Phys. **5**, 76 (2003).

[23] E. Altman, W. Hofstetter, E. Demler, and M. D. Lukin, *Phase Diagram of Two-Component Bosons on an Optical Lattice*, New J. Phys. **5**, 113 (2003).

[24] M. A. Nichols, L. W. Cheuk, M. Okan, T. R. Hartke, E. Mendez, T. Senthil, E. Khatami, H. Zhang, and M. W. Zwierlein, *Spin Transport in a Mott Insulator of Ultracold Fermions*, Science **363**, 383 (2019).

[25] T. Fukuhara *et al.*, *Quantum Dynamics of a Mobile Spin Impurity*, Nat. Phys. **9**, 235 (2013).

[26] T. Fukuhara, P. Schauß, M. Endres, S. Hild, M. Cheneau, I. Bloch, and C. Gross, *Microscopic Observation of Magnon Bound States and Their Dynamics*, Nature (London) **502**, 76 (2013).

[27] S. Hild, T. Fukuhara, P. Schauss, J. Zeiher, M. Knap, E. Demler, I. Bloch, and C. Gross, *Far-from-Equilibrium Spin Transport in Heisenberg Quantum Magnets*, Phys. Rev. Lett. **113**, 147205 (2014).

[28] R. C. Brown, R. Wyllie, S. B. Koller, E. A. Goldschmidt, M. Foss-Feig, and J. V. Porto, *Two-Dimensional Superexchange-Mediated Magnetization Dynamics in an Optical Lattice*, Science **348**, 540 (2015).

[29] L. W. Cheuk, M. A. Nichols, K. R. Lawrence, M. Okan, H. Zhang, and M. W. Zwierlein, *Observation of 2D Fermionic Mott Insulators of* ^{40}K *with Single-Site Resolution*, Phys. Rev. Lett. **116**, 235301 (2016).

[30] M. F. Parsons, A. Mazurenko, C. S. Chiu, G. Ji, D. Greif, and M. Greiner, *Site-Resolved Measurement of the Spin-Correlation Function in the Fermi-Hubbard Model*, Science **353**, 1253 (2016).

[31] A. Mazurenko, C. S. Chiu, G. Ji, M. F. Parsons, M. Kanász-Nagy, R. Schmidt, F. Grusdt, E. Demler, D. Greif, and M. Greiner, *A Cold-Atom Fermi-Hubbard Antiferromagnet*, Nature (London) **545**, 462 (2017).

[32] P. N. Jepsen, J. Amato-Grill, I. Dimitrova, W. W. Ho, E. Demler, and W. Ketterle, *Spin Transport in a Tunable Heisenberg Model Realized with Ultracold Atoms*, Nature (London) **588**, 403 (2020).

[33] J. Spalek, *t-J Model Then and Now: A Personal Perspective from the Pioneering Times*, Acta Phys. Pol. A **111**, 409 (2007).

[34] F. C. Zhang and T. M. Rice, *Effective Hamiltonian for the Superconducting Cu Oxides*, Phys. Rev. B **37**, 3759 (1988).

[35] P. W. Anderson, P. A. Lee, M. Randeria, T. M. Rice, N. Trivedi, and F. C. Zhang, *The Physics behind High-Temperature Superconducting Cuprates: The Plain Vanilla Version of RVB*, J. Phys. Condens. Matter **16**, R755 (2004).

[36] M. Koschorreck, D. Pertot, E. Vogt, and M. Köhl, *Universal Spin Dynamics in Two-Dimensional Fermi Gases*, Nat. Phys. **9**, 405 (2013).

[37] S. Trotzky, S. Beattie, C. Luciuk, S. Smale, A. B. Bardon, T. Enss, E. Taylor, S. Zhang, and J. H. Thywissen, *Observation of the Leggett-Rice Effect in a Unitary Fermi Gas*, Phys. Rev. Lett. **114**, 015301 (2015).

[38] V. Popkov, X. Zhang, and A. Klümper, *Phantom Bethe Excitations and Spin Helix Eigenstates in Integrable Periodic and Open Spin Chains*, Phys. Rev. B **104**, L081410 (2021).

[39] X. Zhang, A. Klümper, and V. Popkov, *Phantom Bethe Roots in the Integrable Open Spin-*$\frac{1}{2}$ *XXZ Chain*, Phys. Rev. B **103**, 115435 (2021).

[40] I. Dimitrova, N. Jepsen, A. Buyskikh, A. Venegas-Gomez, J. Amato-Grill, A. Daley, and W. Ketterle, *Enhanced Superexchange in a Tilted Mott Insulator*, Phys. Rev. Lett. **124**, 043204 (2020).

[41] C. L. Degen, F. Reinhard, and P. Cappellaro, *Quantum Sensing*, Rev. Mod. Phys. **89**, 035002 (2017).

[42] C. P. Slichter, *Principles of Magnetic Resonance*, Springer Series in Solid-State Sciences (Springer, Berlin, 1990).

[43] The prefactor 1.14 is somewhat arbitrarily obtained by integrating the probability for a localized particle to be on the original site, $J_0[t/(\hbar/2\tilde{t})]^2$ to the first zero of the Bessel function J_0.

[44] B. J. Verhaar, E. G. M. van Kempen, and S. J. J. M. F. Kokkelmans, *Predicting Scattering Properties of Ultracold Atoms: Adiabatic Accumulated Phase Method and Mass Scaling*, Phys. Rev. A **79**, 032711 (2009).

[45] G. Martinez and P. Horsch, *Spin Polarons in the t-J Model*, Phys. Rev. B **44**, 317 (1991).

[46] J. Hauschild and F. Pollmann, *Efficient Numerical Simulations with Tensor Networks: Tensor Network Python (TeNPy)*, SciPost Phys. Lect. Notes **5** (2018). . Code available from https://github.com/tenpy/tenpy.

[47] D. V. Else, W. W. Ho, and P. T. Dumitrescu, *Long-Lived Interacting Phases of Matter Protected by Multiple Time-Translation Symmetries in Quasiperiodically Driven Systems*, Phys. Rev. X **10**, 021032 (2020).